PNAS RESEARCH ARTICLE | APPLIED PHYSICAL SCIENCES

Free-electron resonance transition radiation via Brewster randomness

Zheng Gong[a,b], Ruoxi Chen[a,b], Zun Wang[c], Xiangfeng Xi[a,b], Yi Yang[d], Baile Zhang[e,f,1], Hongsheng Chen[a,b,g,h,1], Ido Kaminer[i], and Xiao Lin[a,b,1]

Affiliations are included on p. 7.

Edited by Hui Cao, Yale University, New Haven, CT; received July 3, 2024; accepted December 30, 2024

Free-electron radiation, such as Cherenkov radiation and transition radiation, can generate light at arbitrary frequencies and is fundamental to diverse applications, ranging from electron microscopy, spectroscopy, lasers, to particle detectors. Generally, the features of free-electron radiation are stochastic when electrons interact with random media. Counterintuitively, here, we reveal a type of free-electron radiation that has both its intensity and directionality invariant to specific sorts of long-range structural randomness. Essentially, this invariance is enabled by the Brewster effect and the judiciously engineered phase coherence condition of emitted light, namely that the light induced by electron's penetration through a layered aperiodic nanostructure is engineered to interfere constructively at the Brewster angle. As such, when each constituent layer with a random thickness fulfills this phase coherence condition, there is always the emergence of free-electron resonance transition radiation at the Brewster angle. At this resonant Brewster angle, we further find that the radiation intensity and directionality could be enhanced by orders of magnitude by readily increasing the interface number. The revealed resonance transition radiation via long-range Brewster randomness may offer a feasible route to explore more enticing photonic applications driven by free electrons, such as light sources at previously unreachable spectral regimes, optical frequency combs, particle detectors, and random lasers.

free-electron radiation | random media | Brewster effect | resonance transition radiation | random laser

Significance

Light emission from random media, e.g., free-electron radiation, is widely believed to have stochastic optical features. Here, we break this long-held belief by revealing an exotic type of free-electron radiation that has both its intensity and directionality at a predefined working wavelength invariant to specific sorts of structural randomness, when considering relatively small material losses. Remarkably, this anomalous invariance-to-randomness correspondence could still emerge even in the presence of both long-range and short-range randomness. We further reveal that this surprising resonant phenomenon of light emission essentially arises from the combination of three seemingly disjoint phenomena: Brewster effect, random media, and free-electron radiation. Accordingly, our finding indicates exciting possibilities of reshaping free-electron radiation via random media in a controllable and flexible way.

Free-electron radiation (1–7), as an elementary emission mechanism of light, is of fundamental relevance to many diverse scientific realms, such as nuclear physics and cosmology (8–11). One paradigmatic example is Cherenkov radiation (8, 12–22), which is the characteristic bluish glow of water-cooled nuclear reactors and would emerge when a charged particle (e.g., a swift electron) moves faster than the phase velocity of light in the surrounding matter. Another paradigmatic example of free-electron radiation is transition radiation (23–32), which contributes significantly to the radio emission of the Earth, the Sun, and many interstellar and interplanetary media (33, 34) and occurs whenever a charged particle moves across an optical interface. Up to now, the free-electron radiation has enabled many practical applications, including electron microscopy (35–40), free-electron lasers (41–43), particle detection (44–49), beam diagnostics (50, 51), quantum information processing (19, 52), and medical therapy (53, 54), mainly due to its unique capability to create light emission at arbitrary desired spectral regimes.

Generally, the features of free-electron radiation are random if free electrons interact with random media. The underlying reason is that the random media with either long-range or short-range randomness would give rise to complex yet stochastic multiple scattering of light. On the one hand, it is well known that both short and long-range randomness in photonic structures might create optical scattering and eventual opacity, due to Anderson-localization-type phenomena (55–58). On the other hand, the Debye–Waller effect (59, 60) explains how short-range random fluctuations in periodic structures (e.g., those in atomic crystals caused by thermal motion) could preserve coherence but would cause the attenuation of scattering amplitude, for example, during the diffraction process of X-rays, electrons or neutrons. In short, the occurrence of stochastic scattering of light unavoidably makes the prediction and then the manipulation of free-electron radiation from random media challenging (61–65).

Despite the long research history of free-electron radiation (66–72) and randomness in photonic structures (55–57, 60, 73–75), the investigation of free-electron radiation from random media is still in its infancy and mainly focused on the short-range randomness (76–78). Generally, the short-range randomness, which still preserves the long-range order, does not inhibit the conventional mechanisms of free-electron radiation, since free-electron radiation occurs in a nonlocal fashion (78). Accordingly, the short-range

Author contributions: Z.G. and X.L. designed research; Z.G. performed research; Z.G., R.C., Z.W., X.X., Y.Y., B.Z., H.C., I.K., and X.L. analyzed data; B.Z., H.C., and I.K. supervised the project; and Z.G. and X.L. wrote the paper.

The authors declare no competing interest.

This article is a PNAS Direct Submission.

[1]To whom correspondence may be addressed. Email: blzhang@ntu.edu.sg, hansomchen@zju.edu.cn, or xiaolinzju@zju.edu.cn.

This article contains supporting information online at https://www.pnas.org/lookup/suppl/doi:10.1073/pnas.2413336122/-/DCSupplemental.

Published February 5, 2025.

randomness was found capable to spatially and spectrally shape the free-electron radiation, such as the manipulation of free-electron Smith-Purcell radiation (79–82) via aperiodic nanostructures (76, 77). Till now, there remains an active interest in the role of randomness in free-electron radiation, partly due to the existence of many open scientific questions. Particularly, whether there are specific sorts of structural randomness, especially those with long-range randomness, that could enable some invariant features of free-electron radiation remains elusive.

Here, we reveal an enticing possibility to create some *invariant* features (i.e., the characteristic intensity and directionality of emitted light) of free-electron radiation via *random* media. Remarkably, this invariance-to-randomness correspondence of free-electron radiation would still emerge even in presence of long-range randomness. This finding indicates an exotic randomness-enabled way to significantly improve the performance (e.g., intensity and directionality) of free-electron radiation, for example, by increasing the interface number. The continual exploration of this invariance-to-randomness correspondence might inspire disruptive ways to control light–matter interactions and is of great interdisciplinary interest. As background, the randomness-to-randomness correspondence is indeed universal not only in free-electron radiation and photonics but also in other realms of physics, technology, and even philosophy (58, 83–85).

At the core of this work lies the paradigm to achieve the free-electron resonance transition radiation from random layered aperiodic nanostructures with the aid of Brewster effect. The Brewster effect (30, 86–93), dating back to the pioneering work of Sir David Brewster in the early 1810s, describes a total transmission phenomenon through a dielectric interface under the incidence of *p*-polarized light at the so-called Brewster angle. Recently, it was reported that the Brewster effect can provide a unique route to tailor free-electron radiation, such as the usage of the Brewster effect from stacks of variable one-dimensional photonic crystals to angularly filter the Cherenkov radiation (93) and the usage of the pseudo-Brewster effect from a gain dielectric slab to enhance both the intensity and directionality of transition radiation (30). While these previous studies are limited to the framework of either ordered (30) or locally ordered (93) nanostructures, the intricate interplay between the Brewster effect in aperiodic nanostructures with the long-range randomness and the resonance transition radiation remains unexplored. Essentially, our revealed invariance-to-randomness correspondence for free-electron radiation is achieved by simultaneously enforcing the Brewster effect and a judiciously designed phase coherence condition of emitted light. In other words, the multiple transition radiation created at adjacent interfaces is engineered to interfere constructively at the Brewster angle. Then, if each constituent layer with a random thickness is designed to fulfill this phase coherence condition, we find that there is always the formation of resonance transition radiation at the Brewster angle, whose intensity and directionality are robust to the random variations of each layer thickness. Accordingly, this special sort of structural variation with the long-range randomness is suggested to be termed the Brewster randomness, owing to the fundamental role of Brewster effect. Our revealed Brewster randomness indicates the intriguing potential to reshape free-electron radiation from random media in a controllable and flexible way.

Results

We begin with the introduction on how to construct the Brewster randomness for free-electron resonance transition radiation. As schematically shown in Fig. 1*A*, the swift electron with a velocity $\overline{v} = \hat{z}v$ perpendicularly penetrates through a layered aperiodic nanostructure composed of alternating dielectrics I and II (94–97). In practice, in order to avoid the inelastic electron scattering, a tiny hole with its center along the trajectory of electron could be drilled inside the designed sample (98, 99). For conceptual brevity, the electron velocity is chosen to have $v < \min\left(c/\sqrt{\varepsilon_{\mathrm{r,I}}}, c/\sqrt{\varepsilon_{\mathrm{r,II}}}\right)$, such that the Cherenkov radiation is fully prohibited, where c is the light speed in vacuum, $\varepsilon_{\mathrm{r,X}}$ is the relative permittivity of dielectric X, and X = I or II. In other words, there is only the emergence of transition radiation in this work, which is purely *p*-polarized.

According to the Brewster effect, the *p*-polarized transition radiation would totally transmit through the adjacent interface between dielectrics I and II in Fig. 1*B*, when it propagates along the Brewster angle $\theta_{\mathrm{B,X}} = \arccos\sqrt{\frac{\varepsilon_{\mathrm{r,X}}}{\varepsilon_{\mathrm{r,I}}+\varepsilon_{\mathrm{r,II}}}}$ inside dielectric X. Enabled by this unique capability of Brewster effect, the phase difference between multiple transition radiation emanating from different optical interfaces at the Brewster angle can be readily calculated by exploiting the geometric optics in Fig. 1 *C* and *D*. To be specific, the phase difference $\Delta\varphi$ between the forward-propagating transition radiation from the interface of $z = z_{j-1}$ and that from the interface of $z = z_j$ at the Brewster angle can be analytically obtained as

$$\Delta\varphi = \omega d_{\mathrm{X}}/v - \pi - k_{z,\mathrm{X}} d_{\mathrm{X}}, \qquad [1]$$

where $k_{z,\mathrm{X}} = \frac{\omega}{c} \cdot \frac{\varepsilon_{\mathrm{r,X}}}{\sqrt{\varepsilon_{\mathrm{r,I}}+\varepsilon_{\mathrm{r,II}}}}$ is the z-component wavevector of light propagating along the Brewster angle in dielectric X, $d_{\mathrm{X}} = z_j - z_{j-1}$ is the thickness of the corresponding layer composed of dielectric X, and ω is the angular frequency.

If the phase coherence condition of $\mathrm{mod}(\Delta\varphi, 2\pi) = 0$ is fulfilled, the multiple transition radiation from different optical interfaces would interfere constructively. As a result, the resonance transition radiation would emerge and manifest itself as plane-like waves propagating along the Brewster angle in the forward vacuum region (i.e., region $N + 1$ in Fig. 1*E*). According to this phase coherence condition, the corresponding layer thickness could be obtained as

$$d_{\mathrm{X}} = \left(2m_{\mathrm{X}} + 1\right) \cdot d_{\mathrm{B,X}}, \qquad [2]$$

$$d_{\mathrm{B,X}} = \frac{\lambda}{2\left(c/v - \varepsilon_{\mathrm{r,X}}/\sqrt{\varepsilon_{\mathrm{r,I}}+\varepsilon_{\mathrm{r,II}}}\right)}, \qquad [3]$$

where $m_{\mathrm{X}} \geq 0$ is a random integer and $\lambda = 2\pi c/\omega$ is the wavelength of light in free space. Once the thickness of each constituent layer is randomly chosen but governed by Eqs. **2** and **3**, the designed layered aperiodic nanostructure has the Brewster randomness. According to Eqs. **2** and **3**, the proposed Brewster randomness belongs to a specific sort of long-range randomness (85), without the consideration of short-range disorders (e.g., those caused by imperfect sample fabrications). Actually, the addition of short-range disorders into the designed layered nanostructure would not inhibit the exotic capability of Brewster randomness in the manipulation of free-electron radiation (*SI Appendix*, Figs. S3–S5). For conceptual demonstration, the discussion below focuses on the Brewster randomness described by Eqs. **2** and **3**.

The validity of Eqs. **2** and **3** can be further verified by analyzing the angular spectral energy density of free-electron radiation from layered nanostructures at a predefined working wavelength of $\lambda = \lambda_0$ (e.g., $\lambda_0 = 500$ nm) in Fig. 2. The angular spectral energy

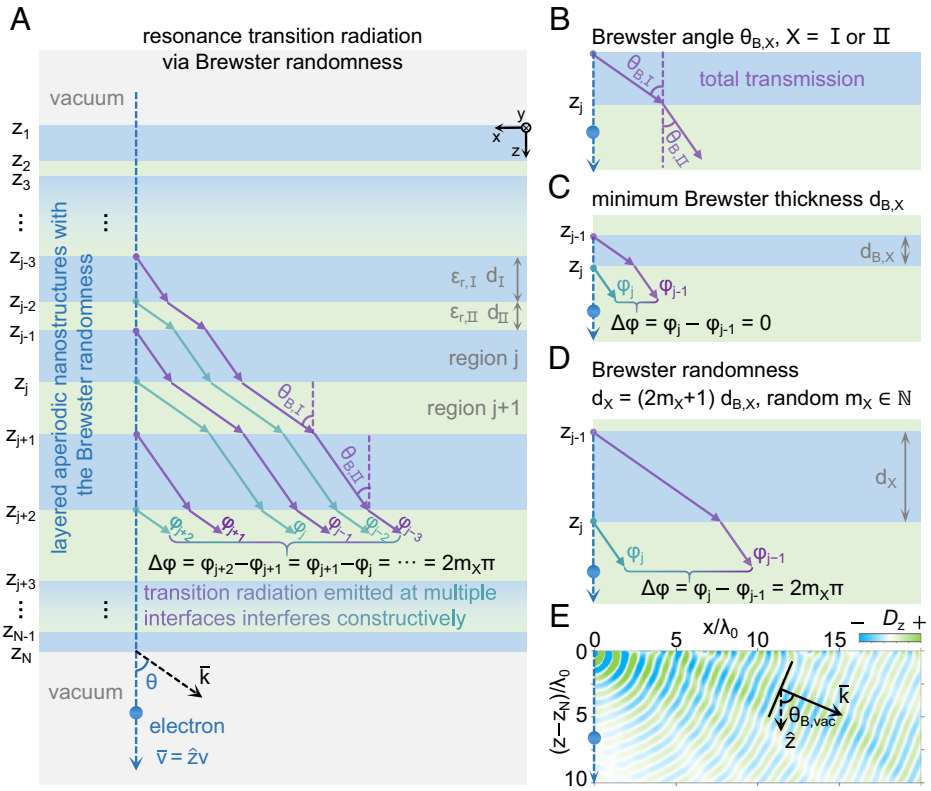

Fig. 1. Conceptual demonstration of free-electron resonance transition radiation from a layered aperiodic nanostructure with Brewster randomness. (*A–D*) Structural schematic for the design of layered aperiodic nanostructures. The layered nanostructure in *A* has *N* parallel interfaces and is composed of two alternating dielectrics, namely dielectric I and dielectric II. Each dielectric has a relative permittivity $\epsilon_{r,X}$ and a thickness d_X, where X = I or II. If the emitted light propagates at the Brewster angle $\theta_{B,X}$ in dielectric X, as depicted in *B*, it could totally transmit through the adjacent interface between dielectric I and II. Meanwhile, the light emitted from the interface of $z = z_j$ and forward propagating in region *J* has a phase φ_j in *C* and *D*, where *j* and *J* are both integers and $J > j$. If the phase coherence condition of $\Delta\varphi = \varphi_j - \varphi_{j-1} = 2m_X\pi$ is fulfilled, all transmitted light at the Brewster angle in region *J* would interfere constructively, where $m_X \geq 0$ is a random interger. If the thickness of each dielectric layer is designed to fulfill this phase coherence condition, the resonance transition radiation could be formed at the Brewster angle. Then, this judiciously engineered layered nanostructure is termed to have the Brewster randomness. For the Brewster randomness, the minimum thickness of dielectric X could be obtained by letting $m_X = 0$ in the phase coherence condition, and it is set to be $d_X = d_{B,X}$ in *C*. When $m_X \neq 0$, we further have $d_X = (2m_X+1)d_{B,X}$ in *D*. (*E*) Field distribution of free-electron resonance transition radiation via the Brewster randomness in region $N+1$. Without further specification, for all the figures in the main text, we set $N = 100$, $\epsilon_{r,I} = 2.1$ [e.g., SiO_2 (94)], $\epsilon_{r,II} = 1.4$ [e.g., ZrO_2 aerogel (95)], the particle velocity $v = v_0 = 0.3c < \min\left(c/\sqrt{\epsilon_{r,I}}, c/\sqrt{\epsilon_{r,II}}\right)$ to avoid the Cherenkov radiation, the surrounding environment being vacuum, m_X being randomly distributed from 0 to 9, and the working wavelength $\lambda = \lambda_0 = 500$ nm.

density $U(\lambda, \theta)$ in Fig. 2 is derived by extending Ginzburg and Frank's theory of transition radiation (23, 25), where θ is the radiation angle in the forward vacuum region. For illustration, the thickness of all layers composed of dielectric II is chosen to be the same inside the whole layered nanostructure, such as $d_{II} \equiv d_{B,II}$ in Fig. 2*A*, which already satisfies Eqs. **2** and **3**. Without loss of generality, the thickness of each layer composed of dielectric I in Fig. 2*A* is set to be $d_I = (2\,m_I+1)d_{0,I}$, where $d_{0,I}$ is a fixed constant but m_I is a random integer from the top to the bottom of the layered nanostructure. Under this scenario, only if $d_{0,I}/d_{B,I}$ is an odd integer, the thickness of all layers composed of dielectric I would satisfy Eqs. **2** and **3**, and then, the designed layered nanostructure has the Brewster randomness.

We find that irrespective of the randomness of m_I, the resonance transition radiation emerges at $\theta = \theta_{B,vac}$ for $d_{0,I}/d_{B,I} = 1$ in Fig. 2*B*, where the angle $\theta_{B,vac} = \arccos\sqrt{\frac{\epsilon_{r,I}\epsilon_{r,II}}{\epsilon_{r,I}+\epsilon_{r,II}}}$ corresponds to the Brewster angle in the forward vacuum region. More generally, there is the emergence of strong radiation peaks in Fig. 2*C* if $d_{0,I}/d_{B,I}$ is an odd integer, which clearly indicates that the Brewster randomness can always give rise to the resonance transition radiation with high directionality at the Brewster angle. Upon close inspection of Eqs. **2** and **3**, the layer thickness used for the construction of Brewster randomness is also sensitive to the electron velocity, as shown in Fig. 2*D*. In addition, if $d_X/d_{B,X}$ is an even integer, the multiple transition radiation created at adjacent interfaces would interfere destructively, leading to the formation of radiation dips in Fig. 2 *C* and *D* and *SI Appendix*, Fig. S6.

With the knowledge of how to construct the Brewster randomness, Fig. 3 investigates the interaction of free electrons with various Brewster randomness in the λ-θ parameter space, which is intrinsically related to the energy–momentum space of emitted light. As governed by Eqs. **2** and **3**, all Brewster randomness in Fig. 3 is designed at a prescribed working wavelength of $\lambda = \lambda_0$ with the usage of $\epsilon_{r,I} = 6.1$ [e.g., $SrTiO_3$ (94)] and $\epsilon_{r,II} = 1$. From the angular spectral energy density, Fig. 3 *A–C* shows that there are a bunch of radiation peaks in the λ-θ parameter space, which can be categorized into three types. First, the appearance of most radiation peaks is intrinsically random and generally sensitive to the variation of Brewster randomness (i.e., the random choice of m_I and m_{II} in Eqs. **2** and **3**). Second, when $\lambda \to \lambda_0$ and $\theta \to \theta_{B,vac} = 67.96°$, the appearance of some radiation peaks in Fig. 3 *A–C* becomes relatively insensitive to the variation of Brewster randomness. We further show in *SI Appendix*, Fig. S7 that the emergence range of these radiation peaks in the energy–momentum space of emitted light can be flexibly tailored through the judicious manipulation

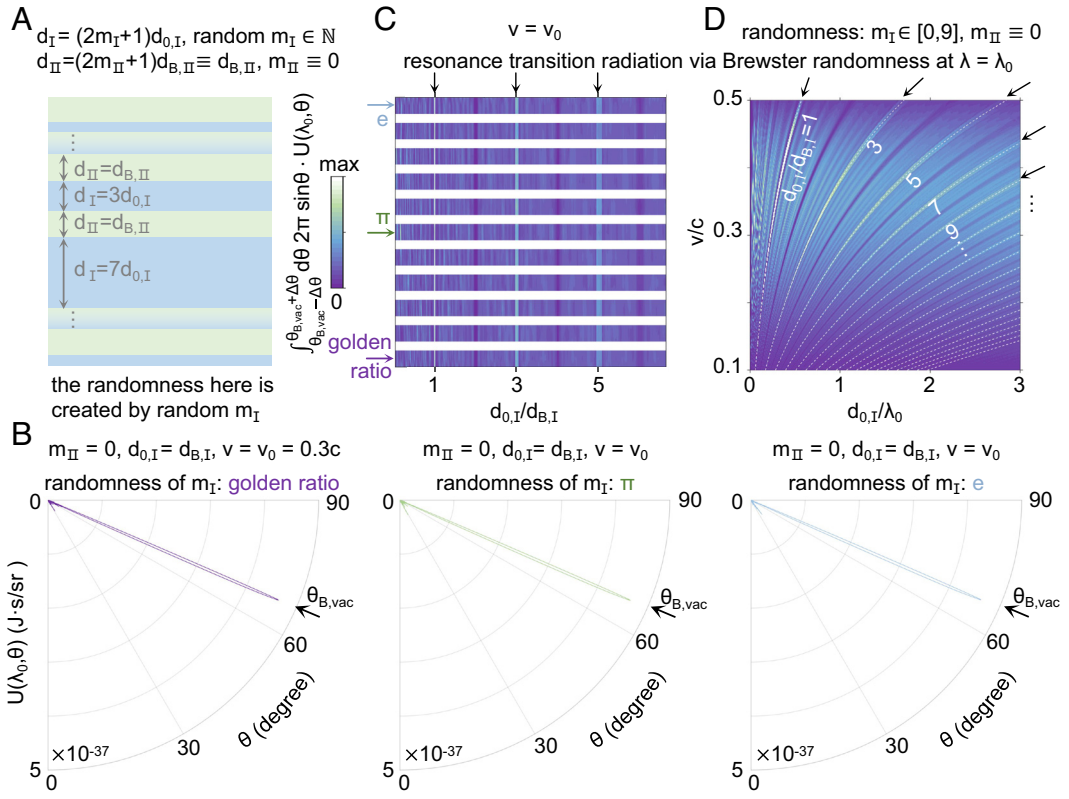

Fig. 2. Angular spectral energy density of free-electron resonance transition radiation via Brewster randomness at a predefined working wavelength $\lambda = \lambda_0$ (e.g., λ_0 = 500 nm in the calculation). For conceptual illustration, here, we use $\varepsilon_{r,I} = 2.1$ and $\varepsilon_{r,II} = 1.4$. (*A*) Structural schematic of the layered aperiodic nanostructure. The thickness of each layer composed of dielectric II is the same inside the whole structure, namely $d_{II} = d_{B,II}$, and the thickness of the layer composed of dielectric I is $d_I = (2m_I+1)d_{0,I}$, where $d_{0,I}$ is a fixed constant and m_I is a random interger. Then, the designed layered aperiodic nanostructure has the Brewster randomness only if $d_{0,I}/d_{B,I}$ is an odd integer. (*B*) Angular spectral energy density $U(\lambda_0, \theta)$ of free-electron forward radiation into region $N+1$, by letting $d_{0,I}/d_{B,I} = 1$. For layers composed of dielectric I, from the top to the bottom, the choice of m_I follows the decimal expansion of some irrational numbers to test various Brewster randomness, such as the golden ratio $(1 + \sqrt{5}/2)$ with m_I = 1, 6, 1, 8... in the *Left* panel, π with m_I = 3, 1, 4, 1... in the *Middle* panel, and Euler's number e with m_I = 2, 7, 1, 8.... in the *Right* panel. (*C*) $\int_{\theta_{B,vac}-\Delta\theta}^{\theta_{B,vac}+\Delta\theta} d\theta(2\pi\sin\theta)U(\lambda_0,\theta)$ as a function of $d_{0,I}$ for various randomness of $m_I \in [0, 9]$ for cases studied in *B* and other cases with computer-generated randomness, under the scenario of $v = v_0 = 0.3c$ and $\Delta\theta = 5°$. (*D*) $\int_{\theta_{B,vac}-\Delta\theta}^{\theta_{B,vac}+\Delta\theta} d\theta(2\pi\sin\theta)U(\lambda_0,\theta)$ as a function of $d_{0,I}$ and v, with computer-generated random integer $m_I \in [0, 9]$.

of material dispersion. Third, strictly speaking, only the radiation peak at the special point of $(l_0, q_{B,vac})$ in Fig. 3 *A–C* is invariant to the variation of Brewster randomness.

To gain a deeper understanding, we extract the dependence of λ_{max} on θ for various Brewster randomness in Fig. 3*D*. This dependence is calculated by using the definition of $U(\lambda_{max}, \theta) = \max[U(\lambda,\theta), \lambda]$ inside a relatively small region, which contains the special point of $(\lambda_0, \theta_{B,vac})$, such as the region with $\lambda/\lambda_0 \in [0.99, 1.01]$ and $\theta \in [64°, 72°]$ in Fig. 3 *A–C*. From Fig. 3*D*, there is always a fixed overlapped point at $\lambda_{max} = \lambda_0$ and $\theta = \theta_{B,vac}$. Meanwhile, Fig. 3*E* shows the dependence of $U(\lambda_{max}, \theta)$ on θ. We find that only the value of $U(\lambda_{max}, \theta_{B,vac})$ in Fig. 3*E* would maintain unchanged under the variation of Brewster randomness. When the radiation angle θ is further away from the Brewster angle $\theta_{B,vac}$, the value of $U(\lambda_{max}, \theta)$ in Fig. 3*E* would become more sensitive to the variation of Brewster randomness.

We now proceed to study the influence of the interface number N on the resonance transition radiation via the Brewster randomness in Fig. 4 *A–E*. Generally, the Brewster angle of $\theta_{B,vac} = \arccos\sqrt{\frac{\varepsilon_{r,I}\varepsilon_{r,II}}{\varepsilon_{r,I}+\varepsilon_{r,II}}}$ at the interface between dielectrics I and II is not equal to the Brewster angle of $\theta'_{B,vac} = \arccos\sqrt{\frac{\varepsilon_{r,I}\varepsilon_{r,II}}{\varepsilon_{r,X}+1}}$ at the interface between dielectric X (X = I or II) and vacuum, when $\varepsilon_{r,X} \neq 1$. This way, there is nonzero reflection at the first and final interfaces of the designed layered nanostructure, despite that the emitted light propagates along the Brewster angle $\theta_{B,X}$ in Fig. 4*A*. Correspondingly, the value of $\mathrm{mod}(\phi_{Brew}, 2\pi)$ would be randomly distributed within the range of $[0, 2\pi)$ in Fig. 4*A*, namely $\mathrm{mod}(\phi_{Brew}, 2\pi) \in [0, 2\pi)$, where $\phi_{Brew}/2 = \sum_{j=2}^{N} k_{z,j}\left(Z_j - Z_{j-1}\right)$ is the accumulated phase during the propagation of light at $\theta = \theta_{B,X}$ from the first interface to the final one. Because of this random phase accumulation, the interference between multiply scattered resonance transition radiation at the forward vacuum region might be randomly constructive or destructive. As a result, Fig. 4*D* shows that the value of $U(\lambda_0, \theta_{B,vac})$ for resonance transition radiation from various Brewster randomness in Fig. 4*A* has an increasing tendency but randomly oscillates with the increasing interface number.

This random-oscillation dependence on the interface number in Fig. 4 *A* and *D* could be detrimental for practical applications. Below, two ways are proposed to eliminate this random oscillation. One way is to add an additional layer composed of dielectric X at the bottom of layered nanostructures with the Brewster randomness in Fig. 4*B*. The thickness of this additional layer does not need to fulfill Eqs. **2** and **3** but should be judiciously designed to enable $\mathrm{mod}(\phi_{Brew}, 2\pi) = 0$, where the accumulated phase now becomes $\phi_{Brew}/2 = \left[\sum_{j=2}^{N} k_{z,j}\left(Z_j - Z_{j-1}\right)\right] + k_{z,N+1}$

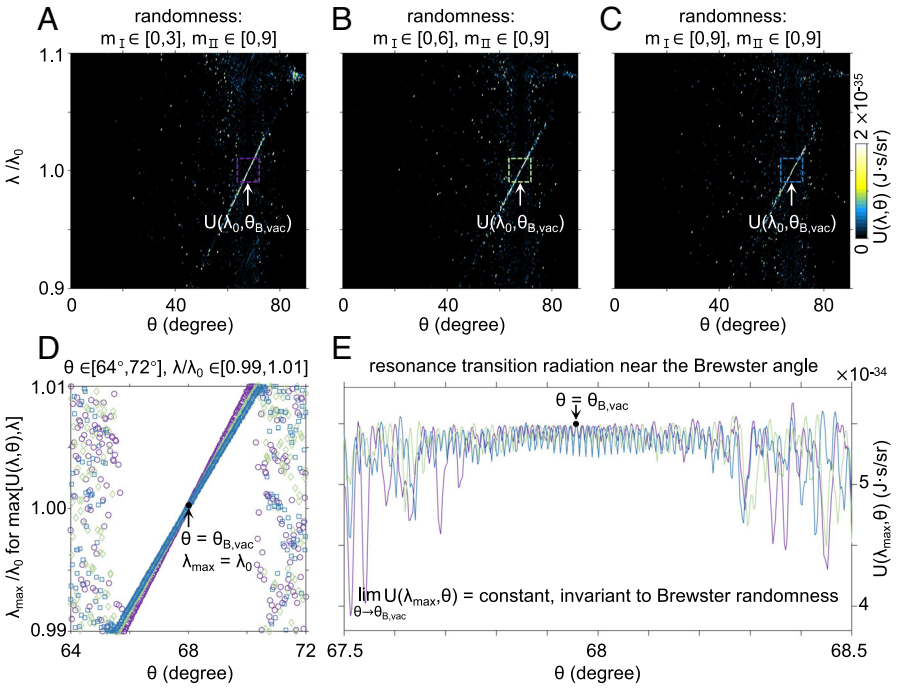

Fig. 3. Free-electron resonance transition radiation via Brewster randomness in the energy–momentum space. The energy–momentum space is equivalent to the λ-θ parameter space, since the working wavelength λ and the radiation angle θ are related to the photon energy $E_{photon} = 2\pi\hbar c/\lambda$ and the component of photon momentum parallel to the interface $p_{||} = \sin\theta \bullet 2\pi\hbar/\lambda$, respectively. (*A*–*C*) Angular spectral energy density $U(\lambda, \theta)$ of free-electron forward radiation from layered aperiodic nanostructures with various Brewster randomness. For illustration, the layered aperiodic nanostructure here has N = 1,000, $\varepsilon_{r,I}$ = 6.1 [e.g., $SrTiO_3$ (94)] and $\varepsilon_{r,II}$ = 1. (*D*) Dependence of λ_{max} on θ for various Brewster randomness, as extracted from *A*–*C*. To be specific, λ_{max} is calculated by using $U(\lambda_{max}, \theta) = \max U(\lambda, \theta), \lambda]$ inside the region of $\lambda/\lambda_0 \in [0.99, 1.01]$ and $\theta \in [64°, 72°]$, which corresponds to the region highlighted by a dashed rectangle in *A*–*C*. (*E*) Dependence of $U(\lambda_{max}, \theta)$ on θ. The value of $U(\lambda_0, \theta_{B,vac})$ is a constant regardless of Brewster randomness.

$(Z_{N+1} - Z_N) = \sum_{j=2}^{N+1} k_{z,j}(Z_j - Z_{j-1})$. Under this scenario, the multiply scattered resonance transition radiation at the forward vacuum region would be all in-phase and then interfere constructively. As a result, Fig. 4*D* shows that the value of $U(\lambda_0, \theta_{B,vac})$ for resonance transition radiation from various Brewster randomness in Fig. 4*B* is proportional to N^2, namely $U(\lambda_0, \theta_{B,vac}) \propto N^2$, when the interface number is $N \gg 1$ (e.g., $N > 100$). Similarly, if the thickness of this additional layer is designed to have $\mathrm{mod}(\phi_{Brew}, 2\pi) = \pi$ in Fig. 4*B*, the destructive interference would always happen for these multiply scattered resonance transition radiation at the forward vacuum region. By comparing the two cases with $\mathrm{mod}(\phi_{Brew}, 2\pi) = 0$ or π in Fig. 4 *B* and *D* further shows that when $N \gg 1$, the judicious design of this additional layer could improve the radiation intensity by one order of magnitude, which is favorable in practical applications.

The other way is to let one of the constituent dielectrics be vacuum (e.g., $\varepsilon_{r,II} = 1$) in Fig. 4*C*. This way, we have $\theta_{B,X} = \theta'_{B,X}$, and there is zero reflection at the first and final interfaces of the designed layered nanostructure in Fig. 4*C*. As a result, Fig. 4*D* shows that the case in Fig. 4*C* has $U(\lambda_0, \theta_{B,vac}) \propto N^2$ for arbitrary interface number N. In this case, Fig. 4*E* shows the dependence of the angular width $\Delta\theta_{FWHM}$ and the spectral width $\Delta\lambda_{FWHM}$ on the interface number, where $\Delta\theta_{FWHM}$ and $\Delta\lambda_{FWHM}$ are the full width at half maximum (FWHM) of $U(\lambda_0, \theta)$ and $U(\lambda, \theta_{B,vac})$, respectively. From Fig. 4*E*, both the angular width and the spectral width are proportional to $1/N$, namely $\Delta\lambda_{FWHM} \propto 1/N$ and $\Delta\theta_{FWHM} \propto 1/N$, if $N \gg 1$. We further show in *SI Appendix*, Fig. S9 the influence of material loss on these revealed relations (e.g., $U(\lambda_0, \theta_{B,vac}) \propto N^2$ and $\Delta\theta_{FWHM} \propto 1/N$) and find that these relations would keep almost unchanged when both the material loss and N are reasonably large. This further indicates the possibility to extend the revealed phenomenon of resonance transition radiation via Brewster randomness from all-dielectric systems studied to other plasmonic and photonic systems (3, 100, 101), once the material loss is reasonably large.

Discussion

In conclusion, we have revealed that the free-electron resonance transition radiation from layered aperiodic nanostructures could have both its intensity and directionality invariant to the long-range Brewster randomness. This invariance-to-randomness correspondence of free-electron radiation from random media might inspire disruptive ways to control light-matter interactions and facilitate the development of miniaturized optical devices driven by free electrons. For example, with the aid of optical broadband angular filter (89, 102–104), the revealed resonance transition radiation via Brewster randomness may enable the exploration of advanced light sources at some previously unreachable spectral regimes (e.g., terahertz, far-infrared, and mid-infrared), simultaneously with high directionality and narrow frequency bandwidth. If a series of layered nanostructures with the Brewster randomness are designed to work at various equally spaced frequencies and then stacked together, a more-complex layered nanostructure with multiple Brewster randomness would be formed, and its interaction with free electrons might give rise to optical frequency combs (105–108). Meanwhile, if the optical gain is introduced into the design of layered nanostructures, the resultant Brewster randomness with optical gain might be exploited for the realization of random lasers (83, 109–111). These optical devices driven by the interactions between free-electrons and the Brewster randomness could be of paramount importance to practical applications,

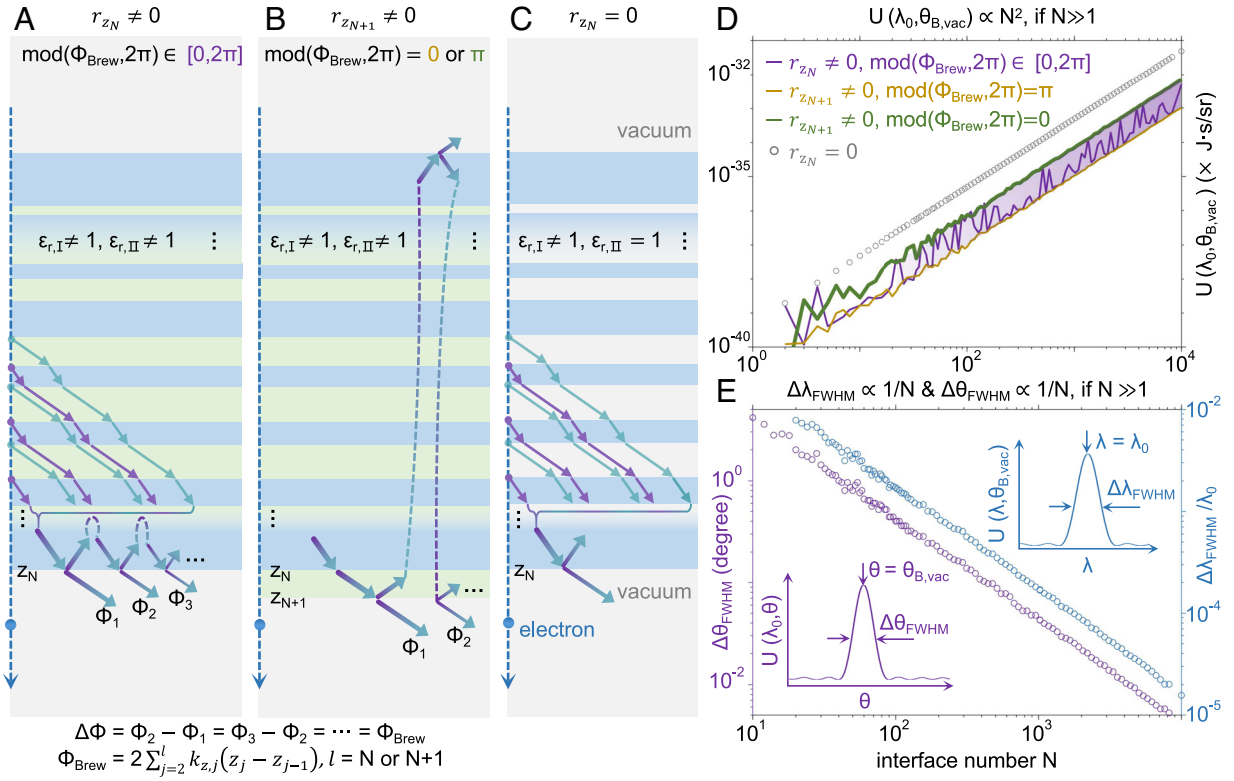

Fig. 4. Dependence of the intensity, angular width, and spectral width of free-electron resonance transition radiation via Brewster randomness on the interface number. (*A–C*) Structural schematic. The layered aperiodic nanostructure with Brewster randomness has $\varepsilon_{r,I} = 3.4$ [e.g., $Y_3Al_5O_{12}$ (94, 96)] in *A–C*, $\varepsilon_{r,II} = 1.4$ [e.g., ZrO_2 aerogel (95)] in *A* and *B* but $\varepsilon_{r,II} = 1$ in *C*. For emitted light with $\theta = \theta_{B,vac}$, there would be nonzero reflection at the first and final interfaces in *A* and *B*, since both $\varepsilon_{r,I}$ and $\varepsilon_{r,II}$ are not equal to one. As a result, $\mathrm{mod}(\phi_{Brew}, 2\pi)$ is generally randomly distributed within the range of $[0, 2\pi)$ in *A*, where $\phi_{Brew}/2$ is the accumulated phase during the propagation of light with $\theta = \theta_{B,vac}$ from the first interface to the final one. Particularly, $\mathrm{mod}(\phi_{Brew}, 2\pi) = 0$ (or π) could be achieved if an additional layer with a judiciously designed thickness is added at the bottom of the layered structure in *B*, and correspondingly, the transmitted forward radiation into region $N + 2$ could interfere constructively (or destructively). By contrast, if $\varepsilon_{r,II} = 1$, there would be zero reflection at the first and final interfaces for emitted light with $\theta = \theta_{B,vac}$ in *C*. (*D*) Dependence of the angular spectral energy density $U(\lambda_0, \theta_{B,vac})$ on the interface number N for cases investigated in *A–C*. (*E*) Dependence of the angular width $\Delta\theta_{FWHM}$ and the spectral width $\Delta\lambda_{FWHM}$ on N for the case investigated in *C*, where $\Delta\theta_{FWHM}$ and $\Delta\lambda_{FWHM}$ correspond to the full width at half maximum (FWHM) of $U(\lambda_0, \theta)$ and $U(\lambda, \theta_{B,vac})$, respectively; see *Insets*.

including on-chip information processing, communications, chemical detection, biomedical sensing, and imaging.

Methods

Derivation of Free-Electron Resonance Transition Radiation from Layered Aperiodic Nanostructures. Within the framework of classical electromagnetics, Ginzburg and Frank's theory of transition radiation from a single interface in *SI Appendix*, Fig. S1 is extended to a layered aperiodic nanostructure with N interfaces in *SI Appendix*, Fig. S2. The angular spectral energy density and excited field distribution of free-electron radiation are analytically derived in *SI Appendix*, section S1. To be specific, the field distribution in real space can be derived by performing the plane-wave expansion, that is, $-E^R(-r,t) = \int d\omega d - k_\perp E^R_{-k_\perp,\omega} e^{i-k_\perp - r_\perp - i\omega t}$. After some calculations, the distribution of radiation field in region j is obtained as

$$E^R_{-k_\perp,\omega,z,j} = \begin{cases} \dfrac{iq}{\omega\varepsilon_0(2\pi)^3}\cdot a_1\cdot e^{-ik_{z,1}(z-d_1)} & (j=1) \\ \dfrac{iq}{\omega\varepsilon_0(2\pi)^3}\left[a_j^-\cdot e^{-ik_{z,j}(z-d_j)} + a_j^+\cdot e^{ik_{z,j}(z-d_{j-1})}\right] & (2\le j\le N)\ , \\ \dfrac{iq}{\omega\varepsilon_0(2\pi)^3}\cdot a_{N+1}\cdot e^{ik_{z,N+1}(z-d_N)} & (j=N+1) \end{cases}$$

where a_j^- (a_j^+) is the generalized factor for the backward (forward) radiation in region j. Based on the knowledge of the radiation field, the forward angular spectral energy density is obtained as $U(\lambda,\theta) = \frac{\varepsilon_{r,N+1}^{3/2} q^2 \cos^2\theta \left|a_{N+1}\right|^2}{4\pi^3\varepsilon_0 c \sin^2\theta}$.

Resonance Transition Radiation via Brewster Randomness at the Brewster Angle. The forward angular spectral energy intensity $U(\lambda_0, \theta_{B,vac})$ of resonance transition radiation via the Brewster randomness at the Brewster angle is analytically obtained in *SI Appendix*, section S2. The dependence of $U(\lambda_0, \theta_{Brew})$ on different parameters, including the interface number, the dielectric permittivities, and the electron velocity, is also analyzed.

Influence of Short-Range Disorders on the Performance of Brewster Randomness. More discussion on the Brewster randomness is provided in *SI Appendix*, section S3, such as the comparison for the long-range Brewster randomness and the short-range structural disorders in *SI Appendix*, Fig. S3, and the influence of short-range structural disorders on the optical features of the revealed resonance transition radiation via the Brewster randomness in *SI Appendix*, Figs. S4 and S5.

More Discussion on the Resonance Transition Radiation via Brewster Randomness. We provide more discussion on the resonance transition radiation via Brewster randomness in *SI Appendix*, section S4, including the destructive interference of multiple transition radiation created at adjacent interfaces in *SI Appendix*, Fig. S6, the influence of material dispersion, material loss, and interface number on the resonance transition radiation via Brewster randomness in *SI Appendix*, Figs. S7–S10, the photon yield of resonance transition radiation via Brewster randomness in *SI Appendix*, Figs. S11 and S12, and the resonance transition radiation via Brewster randomness from layered nanostructures composed of realistic materials in *SI Appendix*, Fig. S13.

Data, Materials, and Software Availability. The data represented in all figures are available on 10.5281/zenodo.14211143 (112). All theoretical and numerical findings can be reproduced based on the information in the article and/or *SI Appendix*.

ACKNOWLEDGMENTS. X.L. acknowledges the support partly from the Fundamental Research Funds for the Central Universities under Grant No. 226-2024-00022, the National Natural Science Fund for Excellent Young Scientists Fund Program (Overseas) of China, the National Natural Science Foundation of China (NSFC) under Grant No. 62475227 and No. 62175212, and Zhejiang Provincial Natural Science Fund Key Project under Grant No. LZ23F050003. H.C. acknowledges the support from the Key Research and Development Program of the Ministry of Science and Technology under Grants No. 2022YFA1404704, 2022YFA1405200, and 2022YFA1404902, the Key Research and Development Program of Zhejiang Province under Grant No.2022C01036, and the Fundamental Research Funds for the Central Universities. R.C. acknowledges the support from the NSFC under Grant No. 623B2089. Y.Y. acknowledges the support from the NSFC Excellent Young Scientists Fund (HKU 12222417), the Hong Kong Research Grant Council Strategic Topics Grant No. STG3/E-704/23-N, the startup fund of The University of Hong Kong, and an Asian Young Scientist Fellowship. B.Z. acknowledges the support from Singapore National Research Foundation Competitive Research Program No. NRF-CRP23-2019-0007.

Author affiliations: [a]Interdisciplinary Center for Quantum Information, State Key Laboratory of Extreme Photonics and Instrumentation, College of Information Science and Electronic Engineering, Zhejiang University, Hangzhou 310027, China; [b]International Joint Innovation Center, The Electromagnetics Academy at Zhejiang University, Zhejiang University, Haining 314400, China; [c]Chu Kochen Honors College, Zhejiang University, Hangzhou 310027, China; [d]Department of Physics, HK Institute of Quantum Science and Technology, The University of Hong Kong, Pokfulam, Hong Kong 999077, China; [e]Division of Physics and Applied Physics, School of Physical and Mathematical Sciences, Nanyang Technological University, Singapore 637371, Singapore; [f]Centre for Disruptive Photonic Technologies, Nanyang Technological University, Singapore 637371, Singapore; [g]Key Laboratory of Advanced Micro/Nano Electronic Devices and Smart Systems of Zhejiang, Jinhua Institute of Zhejiang University, Zhejiang University, Jinhua 321099, China; [h]Shaoxing Institute of Zhejiang University, Zhejiang University, Shaoxing 312000, China; and [i]Department of Electrical and Computer Engineering, Technion-Israel Institute of Technology, Haifa 32000, Israel

1. Y. Yang *et al.*, Free-electron interaction with nonlinear optical states in microresonators. *Science* **383**, 168–173 (2024).
2. Y. Yang *et al.*, Photonic flatband resonances for free-electron radiation. *Nature* **613**, 42–47 (2023).
3. S. Huang *et al.*, Multicolor x-rays from free electron–driven van der Waals heterostructures. *Sci. Adv.* **9**, eadj8584 (2023).
4. A. Karnieli, S. Fan, Jaynes-Cummings interaction between low-energy free electrons and cavity photons. *Sci. Adv.* **9**, eadh2425 (2023).
5. X. Gao, X. Zhao, X. Ma, T. Dong, Free electron emission in vacuum assisted by photonic time crystals. *J. Phys. D Appl. Phys.* **57**, 315112 (2024).
6. C. Roques-Carmes *et al.*, Free-electron–light interactions in nanophotonics. *Appl. Phys. Rev.* **10**, 011303 (2023).
7. Z. Su *et al.*, Manipulating Cherenkov radiation and Smith-Purcell radiation by artificial structures. *Adv. Opt. Mater.* **7**, 1801666 (2019).
8. P. A. Cherenkov, Visible emission of clean liquids by action of gamma radiation. *Dokl. Akad. Nauk SSSR* **2**, 451–454 (1934).
9. W. Galbraith, J. V. Jelley, Light pulses from the night sky associated with cosmic rays. *Nature* **171**, 349–350 (1953).
10. M. Amenomori *et al.*, First detection of photons with energy beyond 100 TeV from an astrophysical source. *Phys. Rev. Lett.* **123**, 051101 (2019).
11. R. Abbasi *et al.*, Observation of high-energy neutrinos from the Galactic plane. *Science* **380**, 1338–1343 (2023).
12. I. E. Tamm, I. M. Frank, Coherent radiation of fast electrons in a medium. *Dokl. Akad. Nauk SSSR* **14**, 107–112 (1937).
13. I. Tamm, Radiation emitted by uniformly moving electrons. *J. Phys. (USSR)* **1**, 439–454 (1939).
14. S. Xi *et al.*, Experimental verification of reversed Cherenkov radiation in left-handed metamaterial. *Phys. Rev. Lett.* **103**, 194801 (2009).
15. S. Liu *et al.*, Surface polariton Cherenkov light radiation source. *Phys. Rev. Lett.* **109**, 153902 (2012).
16. P. Genevet *et al.*, Controlled steering of Cherenkov surface plasmon wakes with a one-dimensional metamaterial. *Nat. Nanotechnol.* **10**, 804–809 (2015).
17. Z. Duan *et al.*, Observation of the reversed Cherenkov radiation. *Nat. Commun.* **8**, 14901 (2017).
18. F. Liu *et al.*, Integrated Cherenkov radiation emitter eliminating the electron velocity threshold. *Nat. Photonics* **11**, 289–292 (2017).
19. Y. Adiv *et al.*, Observation of 2D Cherenkov radiation. *Phys. Rev. X* **13**, 011002 (2023).
20. X. Guo *et al.*, Mid-infrared analogue polaritonic reversed Cherenkov radiation in natural anisotropic crystals. *Nat. Commun.* **14**, 2532 (2023).
21. Z. Gong *et al.*, Interfacial Cherenkov radiation from ultralow-energy electrons. *Proc. Natl. Acad. Sci. U.S.A.* **120**, e2306601120 (2023).
22. Z. Xu *et al.*, Observation of analog flatland Cherenkov radiations on metasurfaces. *Laser. Photon. Rev.* **18**, 2300763 (2024).
23. V. L. Ginzburg, I. M. Frank, Radiation of a uniformly moving electron due to its transition from one medium into another. *J. Phys. (USSR)* **9**, 353–362 (1945).
24. P. Goldsmith, J. V. Jelley, Optical transition radiation from protons entering metal surfaces. *Philos. Mag.* **4**, 836–844 (1959).
25. V. L. Ginzburg, *Transition Radiation and Transition Scattering* (A. Hilger, 1990).
26. S. N. Galyamin, A. V. Tyukhtin, A. Kanareykin, P. Schoessow, Reversed Cherenkov-transition radiation by a charge crossing a left-handed medium boundary. *Phys. Rev. Lett.* **103**, 194802 (2009).
27. I. P. Ivanov, D. V. Karlovets, Detecting transition radiation from a magnetic moment. *Phys. Rev. Lett.* **110**, 264801 (2013).
28. X. Lin *et al.*, Controlling Cherenkov angles with resonance transition radiation. *Nat. Phys.* **14**, 816–821 (2018).
29. Y. Yu *et al.*, Transition radiation in photonic topological crystals: Quasiresonant excitation of robust edge states by a moving charge. *Phys. Rev. Lett.* **123**, 057402 (2019).
30. R. Chen *et al.*, Free-electron Brewster-transition radiation. *Sci. Adv.* **9**, eadh8098 (2023).
31. J. Chen *et al.*, Low-velocity-favored transition radiation. *Phys. Rev. Lett.* **131**, 113002 (2023).
32. R. Chen *et al.*, Recent advances of transition radiation: Fundamentals and applications. *Mater. Today Electron.* **3**, 100025 (2023).
33. G. B. Yodh, X. Artru, R. Ramaty, Transition radiation in astrophysics. *Astrophys. J.* **181**, 725–736 (1973).
34. K. Y. Platonov, G. D. Fleishman, Transition radiation in media with random inhomogeneities. *Phys. Uspekhi* **45**, 235 (2002).
35. A. Feist *et al.*, Quantum coherent optical phase modulation in an ultrafast transmission electron microscope. *Nature* **521**, 200–203 (2015).
36. K. Wang *et al.*, Coherent interaction between free electrons and a photonic cavity. *Nature* **582**, 50–54 (2020).
37. D. Pan, H. Xu, Polarizing free electrons in optical near fields. *Phys. Rev. Lett.* **130**, 186901 (2023).
38. M. Yannai *et al.*, Lossless monochromator in an ultrafast electron microscope using near-field THz radiation. *Phys. Rev. Lett.* **131**, 145002 (2023).
39. Y. Auad *et al.*, μeV electron spectromicroscopy using free-space light. *Nat. Commun.* **14**, 4442 (2023).
40. T. Bucher *et al.*, Free-electron Ramsey-type interferometry for enhanced amplitude and phase imaging of nearfields. *Sci. Adv.* **9**, eadi5729 (2023).
41. P. G. O'Shea, H. P. Freund, Free-electron lasers: Status and applications. *Science* **292**, 1853–1858 (2001).
42. G. Perosa *et al.*, Femtosecond polarization shaping of free-electron laser pulses. *Phys. Rev. Lett.* **131**, 045001 (2023).
43. E. Prat *et al.*, An X-ray free-electron laser with a highly configurable undulator and integrated chicanes for tailored pulse properties. *Nat. Commun.* **14**, 5069 (2023).
44. O. Chamberlain, E. Segrè, C. Wiegand, T. Ypsilantis, Observation of antiprotons. *Phys. Rev.* **100**, 947 (1955).
45. J. J. Aubert *et al.*, Experimental observation of a heavy particle. *J. Phys. Rev. Lett.* **33**, 1404 (1974).
46. P. Bagnaia *et al.*; UA2 Collaboration, Evidence for Z0→ e+ e− at the CERN pp collider. *Phys. Lett. B* **129**, 130–140 (1983).
47. F. Reines, The neutrino: From poltergeist to particle. *Rev. Mod. Phys.* **68**, 317 (1996).
48. ATLAS Collaboration, Observation of a new particle in the search for the Standard Model Higgs boson with the ATLAS detector at the LHC. *Phys. Lett. B* **716**, 1–29 (2012).
49. H. Hu *et al.*, Surface Dyakonov-Cherenkov radiation. *eLight* **2**, 2 (2022).
50. L. Wartski, J. Marcou, S. Roland, Detection of optical transition radiation and its application to beam diagnostics. *IEEE Trans. Nucl. Sci.* **20**, 544–548 (1973).
51. H. Liu *et al.*, Cherenkov radiation-based optical fibre diagnostics of fast electrons generated in intense laser-plasma interactions. *Rev. Sci. Instruments* **89**, 083302 (2018).
52. J. Sloan, N. Rivera, J. D. Joannopoulos, M. Soljačić, Controlling two-photon emission from superluminal and accelerating index perturbations. *Nat. Phys.* **18**, 67–74 (2022).
53. A. K. Glaser, R. Zhang, D. J. Gladstone, B. W. Pogue, Optical dosimetry of radiotherapy beams using Cherenkov radiation: The relationship between light emission and dose. *Phys. Med. Biol.* **59**, 3789 (2014).
54. X. Cui *et al.*, Beyond external light: On-spot light generation or light delivery for highly penetrated photodynamic therapy. *ACS Nano* **17**, 20776–20803 (2023).
55. S. John, Electromagnetic absorption in a disordered medium near a photon mobility edge. *Phys. Rev. Lett.* **53**, 2169 (1984).
56. M. Segev, Y. Silberberg, D. N. Christodoulides, Anderson localization of light. *Nat. Photonics* **7**, 197–204 (2013).
57. A. Yamilov *et al.*, Anderson localization of electromagnetic waves in three dimensions. *Nat. Phys.* **19**, 1308–1313 (2023).
58. P. W. Anderson, Absence of diffusion in certain random lattices. *Phys. Rev.* **109**, 1492 (1958).
59. N. W. Ashcroft, N. D. Mermin, *Solid State Physics* (Harcourt College, 1976).
60. J. Ruze, Antenna tolerance theory–A review. *Proc. IEEE* **54**, 633–640 (1966).
61. S. P. Kapitsa, Radiation from a charge moving in an inhomogeneous medium. *J. Exp. Theor. Phys.* **39**, 1367 (1960).
62. V. V. Tamoykin, Cherenkov and transient radiation of uniformly moving charge in random inhomogeneous medium. *Astrophys. Space Sci.* **16**, 120–129 (1972).
63. K. Y. Platonov, I. Toptygin, G. D. FleÄshman, Emission of radiation by particles in media with inhomogeneities and coherent bremsstrahlung. *Soviet Phys. Uspekhi* **33**, 289 (1990).
64. A. I. Alikhanian, K. M. Avakina, G. M. Garibian, M. P. Lorikian, K. K. Shikhliarov, Detection of X-Ray transition radiation by means of a spark chamber. *Phys. Rev. Lett.* **25**, 635 (1970).
65. Z. S. Gevorkian, Smith-Purcell radiation from rough surfaces. *Phys. Rev. ST Accel. Beams* **13**, 070705 (2010).
66. F. J. G. de Abajo, Optical excitations in electron microscopy. *Rev. Mod. Phys.* **82**, 209 (2010).
67. X. Shi, L. W. W. Wong, S. Huang, L. J. Wong, I. Kaminer, Transverse recoil imprinted on free-electron radiation. *Nat. Commun.* **15**, 7803 (2024).
68. S. Huang *et al.*, Quantum recoil in free-electron interactions with atomic lattices. *Nat. Photonics* **17**, 224–230 (2023).
69. R. Dahan *et al.*, Creation of optical cat and GKP states using shaped free electrons. *Phys. Rev. X* **13**, 031001 (2023).
70. F. J. G. de Abajo, E. J. C. Dias, V. Di Giulio, Complete excitation of discrete quantum systems by single free electrons. *Phys. Rev. Lett.* **129**, 093401 (2022).

71. A. Feist *et al.*, Cavity-mediated electron-photon pairs. *Science* **377**, 777–780 (2022).
72. F. J. G. de Abajo, C. Ropers, Spatiotemporal electron beam focusing through parallel interactions with shaped optical fields. *Phys. Rev. Lett.* **130**, 246901 (2023).
73. S. Zhu *et al.*, Harnessing disordered photonics via multi-task learning towards intelligent four-dimensional light field sensors. *PhotoniX* **4**, 26 (2023).
74. Y. Liu *et al.*, Three-channel robust optical encryption via engineering coherence Stokes vector of partially coherent light. *PhotoniX* **5**, 8 (2024).
75. C. Wang *et al.*, Superscattering of light: Fundamentals and applications. *Rep. Progress Phys.* **87**, 126401 (2024).
76. J. R. M. Saavedra, D. Castells-Graells, F. J. G. de Abajo, Smith–Purcell radiation emission in aperiodic arrays. *Phys. Rev. B* **94**, 035418 (2016).
77. R. Remez *et al.*, Spectral and spatial shaping of Smith–Purcell radiation. *Phys. Rev. A* **96**, 061801 (2017).
78. I. Kaminer *et al.*, Spectrally and spatially resolved Smith–Purcell radiation in plasmonic crystals with short-range disorder. *Phys. Rev. X* **7**, 011003 (2017).
79. F. Chen *et al.*, Tuning Smith–Purcell radiation by rotating a metallic nanodisk array. *Opt. Lett.* **48**, 2002–2005 (2023).
80. Z. Zhang *et al.*, Chiral plasmons enable coherent vortex Smith–Purcell radiation. *Laser. Photon. Rev.* **17**, 2200420 (2023).
81. Z. Su, F. Cheng, L. Li, Y. Liu, Complete control of Smith–Purcell radiation by graphene metasurfaces. *ACS Photonics* **6**, 1947–1954 (2019).
82. Z. Wang, K. Yao, M. Chen, H. Chen, Y. Liu, Manipulating Smith–Purcell emission with babinet metasurfaces. *Phys. Rev. Lett.* **117**, 157401 (2016).
83. R. Sapienza, Controlling random lasing action. *Nat. Phys.* **18**, 976–979 (2022).
84. M. N. Bera, A. Acín, M. Kuś, M. W. Mitchell, M. Lewenstein, Randomness in quantum mechanics: Philosophy, physics and technology. *Rep. Progress Phys.* **80**, 124001 (2017).
85. K. Kim *et al.*, Massively parallel ultrafast random bit generation with a chip-scale laser. *Science* **371**, 948–952 (2021).
86. D. Brewster, On the laws which regulate the polarization of light by reflection from transparent bodies. *Philos. Trans. R. Soc. Lond.* **105**, 125–159 (1815).
87. J. E. Sipe, P. Sheng, B. S. White, M. H. Cohen, Brewster anomalies: A polarization-induced delocalization effect. *Phys. Rev. Lett.* **60**, 108 (1988).
88. Z. Wu, F. Zhai, F. M. Peeters, H. Q. Xu, K. Chang, Valley-dependent Brewster angles and Goos-Hänchen effect in strained graphene. *Phys. Rev. Lett.* **106**, 176802 (2011).
89. Y. Shen *et al.*, Optical broadband angular selectivity. *Science* **343**, 1499–1501 (2014).
90. R. Paniagua-Domínguez *et al.*, Generalized Brewster effect in dielectric metasurfaces. *Nat. Commun.* **7**, 10362 (2016).
91. X. Lin, Y. Shen, I. Kaminer, H. Chen, M. Soljačić, Transverse-electric Brewster effect enabled by nonmagnetic two-dimensional materials. *Phys. Rev. A* **94**, 023836 (2016).
92. Z. Chen *et al.*, Graphene controlled Brewster angle device for ultra broadband terahertz modulation. *Nat. Commun.* **9**, 4909 (2018).
93. X. Lin *et al.*, A Brewster route to Cherenkov detectors. *Nat. Commun.* **12**, 5554 (2021).
94. E. D. Palik, *Handbook of Optical Constants of Solids* (Academic press, 1998).
95. A. Pirvaram, N. Talebzadeh, M. Rostami, S. N. Leung, P. G. O'Brien, Evaluation of a ZrO2/ZrO2-aerogel one-dimensional photonic crystal as an optical filter for thermophotovoltaic applications. *Thermal Sci. Eng. Progress* **25**, 100968 (2021).
96. J. Hrabovský, M. Kučera, L. Paloušová, L. Bi, M. Veis, Optical characterization of Y3Al5O12 and Lu3Al5O12 single crystals. *Opt. Mater. Express* **11**, 1218–1223 (2021).
97. K. Leosson, B. Agnarsson, Integrated biophotonics with CYTOP. *Micromachines* **3**, 114–125 (2012).
98. G. Adamo *et al.*, Light well: A tunable free-electron light source on a chip. *Phys. Rev. Lett.* **103**, 113901 (2009).
99. Z. Dang *et al.*, Chiral Smith-Purcell radiation light source. *Adv. Opt. Mater.* **11**, 2300274 (2023).
100. H. Hu *et al.*, Nonlocality induced Cherenkov threshold. *Laser. Photon. Rev.* **14**, 2000149 (2020).
101. H. Hu *et al.*, Broadband enhancement of Cherenkov radiation using dispersionless plasmons. *Adv. Sci.* **9**, 2200538 (2022).
102. Y. Shen *et al.*, Metamaterial broadband angular selectivity. *Phys. Rev. B* **90**, 125422 (2014).
103. Y. Shen, C. W. Hsu, Y. X. Yeng, J. D. Joannopoulos, M. Soljačić, Broadband angular selectivity of light at the nanoscale: Progress, applications, and outlook. *Appl. Phys. Rev.* **3**, 011103 (2016).
104. Y. Qu *et al.*, Polarization–independent optical broadband angular selectivity. *ACS Photonics* **5**, 4125–4131 (2018).
105. V. Brasch *et al.*, Photonic chip-based optical frequency comb using soliton Cherenkov radiation. *Science* **351**, 357–360 (2016).
106. N. Picqué, T. W. Hänsch, Frequency comb spectroscopy. *Nat. Photonics* **13**, 146–157 (2019).
107. S. A. Diddams, K. Vahala, T. Udem, Optical frequency combs: Coherently uniting the electromagnetic spectrum. *Science* **369**, eaay3676 (2020).
108. L. Chang, S. Liu, J. E. Bowers, Integrated optical frequency comb technologies. *Nat. Photonics* **16**, 95–108 (2022).
109. D. S. Wiersma, The physics and applications of random lasers. *Nat. Phys.* **4**, 359–367 (2008).
110. N. Bachelard, J. Andreasen, S. Gigan, P. Sebbah, Taming random lasers through active spatial control of the pump. *Phys. Rev. Lett.* **109**, 033903 (2012).
111. H. Cao, R. Chriki, S. Bittner, A. A. Friesem, N. Davidson, Complex lasers with controllable coherence. *Nat. Rev. Phys.* **1**, 156–168 (2019).
112. Z. Gong, Free-electron resonance transition radiation via brewster randomness–Data set [Data set]. Zenodo. (2024). https://doi.org/10.5281/zenodo.14211143. Deposited 24 November 2024.

Supplementary Information for

Free-electron resonance transition radiation via Brewster randomness

Zheng Gong, Ruoxi Chen, Zun Wang, Xiangfeng Xi, Yi Yang, Baile Zhang, Hongsheng Chen, Ido Kaminer, and Xiao Lin

Section S1: Derivation of resonance transition radiation from layered aperiodic nanostructures

In this section, we analytically derive the resonance transition radiation from layered aperiodic nanostructures by following Ginzburg and Frank's theory of transition radiation from a single optical interface [1,2]. The derivation below extends our previous work on free-electron radiation from layered periodic nanostructures [3] to the aperiodic case here. We did not resort to the numerical simulation via some commercial softwares (e.g. COMSOL Multiphysics), mainly because the software simulation is neither straightforward nor practical to investigate the phenomena presented in this work. To be specific, when the interface number or total thickness of the designed sample is large, the lateral size of the designed sample should also be large enough, in order to allow for the calculation of the angular spectral energy density of all emitted light into the vacuum region. This way, the volume of the designed sample in the software simulation would be very large, which further requires an extremely large number of meshes in the software simulation to ensure the calculation accuracy. This requirement would unavoidably make the three-dimensional numerical simulation very time-consuming and challenging. This is exactly why we prefer the analytical derivation, which can facilitate the direct calculation of the angular spectral energy density of all emitted light. Actually, after obtaining all necessary analytical formulas, the subsequent calculation would be very straightforward and efficient. On the other hand, we would like to highlight that our analytical framework has been built on a very solid foundation with well-established validity; see our recent progresses on transition radiation in Refs. [3-6]. As a typical example, when a swift electron moves across one-dimensional photonic crystals, we have critically proven that the angular spectral energy density of emitted light matches well with the prediction based on the Bloch band theory (e.g. see Fig. 3 *C* and *D* in Ref. [3]).

S1.1 Transition radiation from a single optical interface

In this subsection, we provide the derivation of transition radiation at a single optical interface in Fig. S1.

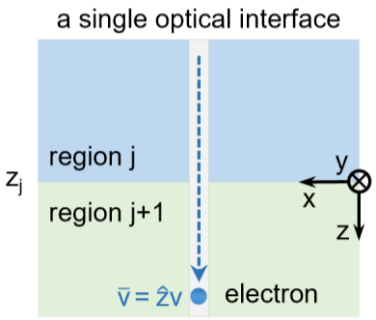

Fig. S1. Structural schematic of transition radiation at a single optical interface

An electron with induced current density $\bar{J}(\bar{r},t)=\hat{z}qv\delta(x)\delta(y)\delta(z-vt)$ perpendicularly penetrates the interface $z=z_j$. To ensure the penetration, a small hole with a subwavelength size is drilled along the electron trajectory.

By performing the plane-wave expansion to the source and all fields, namely

$$\begin{aligned}\bar{J}(\bar{r},t)&=\int d\omega\ d\bar{k}_{\perp}(z)\bar{J}_{\bar{k}_{\perp},\omega}e^{i\bar{k}_{\perp}\bar{r}_{\perp}-i\omega t}\\ \bar{H}(\bar{r},t)&=\int d\omega\, d\bar{k}_{\perp}\bar{H}_{\bar{k}_{\perp},\omega}(z)e^{i\bar{k}_{\perp}\bar{r}_{\perp}-i\omega t}\\ \bar{E}(\bar{r},t)&=\int d\omega\, d\bar{k}_{\perp}\bar{E}_{\bar{k}_{\perp},\omega}(z)e^{i\bar{k}_{\perp}\bar{r}_{\perp}-i\omega t}\end{aligned} \tag{S1}$$

where the excited field has a wavevector of $\bar{k}=\hat{\perp}\,k_{\perp}+\hat{z}k_z$, and the subscript $\perp$ indicates the component of the wavevector perpendicular to the electron velocity. This rule also applies for all physical quantities in the following. From equation (S1), one has $\bar{J}_{\bar{k}_{\perp},\omega}=\hat{z}\frac{q}{(2\pi)^3}e^{i\frac{\omega}{v}z}$. For simplicity, the subscripts $\bar{k}_{\perp}$ and ω are ignored in the following.

By solving Maxwell's equations, the equations that govern H_z and E_z in the medium with permittivity ε and permeability μ are given by

$$\left(\frac{\partial^2}{\partial z^2}+\omega^2\mu\varepsilon+\nabla_{\perp}^2\right)\begin{pmatrix}E_z\\H_z\end{pmatrix}=\begin{pmatrix}-\left(\frac{\partial^2}{\partial z^2}+\omega^2\mu\varepsilon\right)\frac{J_z}{i\omega\varepsilon}-\nabla_{\perp}\cdot\frac{\partial\bar{J}_{\perp}}{\partial z}\\ -\frac{\nabla_{\perp}\cdot\frac{\partial}{\partial z}\bar{J}_{\perp}}{i\omega\mu}\end{pmatrix} \tag{S2}$$

Since $\bar{J}_{\perp}=0$, we have $H_z=0$. This way, all excited fields are transverse-magnetic (TM, or *p*-polarized) waves. Substituting $J_z=\frac{q}{(2\pi)^3}e^{i\frac{\omega}{v}z}$ into equation (S2), we have

$$\begin{aligned}E_z&=E_z^q+E_z^R\\ E_{z,j}^q&=-\frac{iq}{\omega\varepsilon_0(2\pi)^3}\frac{1-\frac{c^2}{v^2\varepsilon_{\mathrm{r},j}}}{\varepsilon_{\mathrm{r}.j}-\frac{c^2}{v^2}-\frac{k_{\perp}^2c^2}{\omega^2}}e^{i\frac{\omega}{v}z}\\ E_{z,j+1}^q&=-\frac{iq}{\omega\varepsilon_0(2\pi)^3}\frac{1-\frac{c^2}{v^2\varepsilon_{\mathrm{r},j+1}}}{\varepsilon_{\mathrm{r}.j+1}-\frac{c^2}{v^2}-\frac{k_{\perp}^2c^2}{\omega^2}}e^{i\frac{\omega}{v}z}\\ E_{z,j}^R&=\frac{iq}{\omega\varepsilon_0(2\pi)^3}a_{j|j+1}^{-}e^{-ik_{z,j}(z-z_j)}\\ E_{z,j+1}^R&=\frac{iq}{\omega\varepsilon_0(2\pi)^3}a_{j|j+1}^{+}e^{ik_{z,j+1}(z-z_j)}\end{aligned} \tag{S3}$$

where c is the speed of light in free space, ε_0 is the permittivity of free space, $\varepsilon_{\mathrm{r},j}$ is the relative permittivity of region j, E^q is the charge field, E^R is the radiation field, and the component of wavevector along z direction in region j is $k_{z,j} = \sqrt{\frac{\omega^2}{c^2}\varepsilon_{\mathrm{r},j} - k_\perp^2}$. Moreover, $a^-_{j|j+1}$ ($a^+_{j|j+1}$) is the factor of the backward (forward) radiation from the $j|j+1$ interface at the plane of $z = z_j$. They can be expressed as

$$\begin{aligned} a^-_{j|j+1} &= a^{-,0}_{j|j+1} e^{i\frac{\omega}{v}z_j} \\ a^+_{j|j+1} &= a^{+,0}_{j|j+1} e^{i\frac{\omega}{v}z_j} \end{aligned} \tag{S4}$$

where $a^{-,0}_{j|j+1}$ ($a^{+,0}_{j|j+1}$) is the factor of the backward (forward) radiation from the $j|j+1$ interface when $z_j = 0$. By matching the boundary conditions at $z = 0$, one has

$$\begin{aligned} a^{-,0}_{j|j+1} &= \frac{-\frac{v}{c}\cdot\frac{k_\perp^2 c^2}{\omega^2}}{\left(\varepsilon_{\mathrm{r},j}\frac{k_{z,j+1}}{\omega/c} + \varepsilon_{\mathrm{r},j+1}\frac{k_{z,j}}{\omega/c}\right)} \cdot \left[\frac{1 - \frac{v}{c}\cdot\frac{k_{z,j+1}}{\omega/c}}{\left(1 - \frac{v^2}{c^2}\varepsilon_{\mathrm{r},j+1} + \frac{k_\perp^2 v^2}{\omega^2}\right)} - \frac{\frac{\varepsilon_{\mathrm{r},j+1}}{\varepsilon_{\mathrm{r},j}} - \frac{v}{c}\cdot\frac{k_{z,j+1}}{\omega/c}}{\left(1 - \frac{v^2}{c^2}\varepsilon_{\mathrm{r},j} + \frac{k_\perp^2 v^2}{\omega^2}\right)}\right] \\ a^{+,0}_{j|j+1} &= \frac{\frac{v}{c}\cdot\frac{k_\perp^2 c^2}{\omega^2}}{\left(\varepsilon_{\mathrm{r},j+1}\frac{k_{z,j}}{\omega/c} + \varepsilon_{\mathrm{r},j}\frac{k_{z,j+1}}{\omega/c}\right)} \cdot \left[\frac{1 + \frac{v}{c}\cdot\frac{k_{z,j}}{\omega/c}}{\left(1 - \frac{v^2}{c^2}\varepsilon_{\mathrm{r},j} + \frac{k_\perp^2 v^2}{\omega^2}\right)} - \frac{\frac{\varepsilon_{\mathrm{r},j}}{\varepsilon_{\mathrm{r},j+1}} + \frac{v}{c}\cdot\frac{k_{z,j}}{\omega/c}}{\left(1 - \frac{v^2}{c^2}\varepsilon_{\mathrm{r},j+1} + \frac{k_\perp^2 v^2}{\omega^2}\right)}\right] \end{aligned} \tag{S5}$$

From equations (S1-S5), one can express the z-component of all fields in the cylindrical coordinates (ρ, ϕ, z), namely

$$\begin{aligned} \bar{E}_z(\bar{r},t) &= \bar{E}_z^q(\bar{r},t) + \bar{E}_z^R(\bar{r},t) \\ \bar{E}^q_{z,j}(\bar{r},t) &= \hat{z}\int_{-\infty}^{\infty} d\omega \frac{-q}{8\pi\omega\varepsilon_0\varepsilon_{\mathrm{r},j}}\left(\frac{\omega^2}{c^2}\varepsilon_{\mathrm{r},j} - \frac{\omega^2}{v^2}\right) H_0^{(1)}\left(\rho\sqrt{\frac{\omega^2}{c^2}\varepsilon_{\mathrm{r},j} - \frac{\omega^2}{v^2}}\right) e^{i\frac{\omega}{v}z - \omega t} \\ \bar{E}^R_{z,j}(\bar{r},t) &= \hat{z}\int_{-\infty}^{\infty} d\omega \int_0^{\infty} dk_\perp \frac{iq}{\omega\varepsilon_0(2\pi)^3} a^-_{j|j+1}\left(2\pi k_\perp J_0(k_\perp\rho)\right) e^{-ik_{z,j}(z - z_j) - i\omega t} \\ \bar{E}^q_{z,j+1}(\bar{r},t) &= \hat{z}\int_{-\infty}^{\infty} d\omega \frac{-q}{8\pi\omega\varepsilon_0\varepsilon_{\mathrm{r},j+1}}\left(\frac{\omega^2}{c^2}\varepsilon_{\mathrm{r},j+1} - \frac{\omega^2}{v^2}\right) H_0^{(1)}\left(\rho\sqrt{\frac{\omega^2}{c^2}\varepsilon_{\mathrm{r},j+1} - \frac{\omega^2}{v^2}}\right) e^{i\frac{\omega}{v}z - \omega t} \\ \bar{E}^R_{z,j+1}(\bar{r},t) &= \hat{z}\int_{-\infty}^{\infty} d\omega \int_0^{\infty} dk_\perp \frac{iq}{\omega\varepsilon_0(2\pi)^3} a^+_{j|j+1}\left(2\pi k_\perp J_0(k_\perp\rho)\right) e^{ik_{z,j+1}(z - z_j) - i\omega t} \end{aligned} \tag{S6}$$

where $H_0^{(1)}$ and $H_1^{(1)}$ represent the first kind of Hankel function of zero order and first order, respectively; J_0 is the first kind of Bessel function of zero order.

S1.2 Interference of multiple transition radiation created at various optical interfaces

In this subsection, we calculate the interference of multiple transition radiation created at various optical interfaces ($j|j+1$ interface, $\forall j = 1,2,\ldots N$. As illustrated in Fig. S2, the total electromagnetic field in region j originates from the interfaces above region j and those below it. We start with the parts 1, 2 and 3 that

originates from the light emission at the interfaces above region j; and the field in region j from the transition radiation at the interfaces below region j is derived in parts 4, 5 and 6.

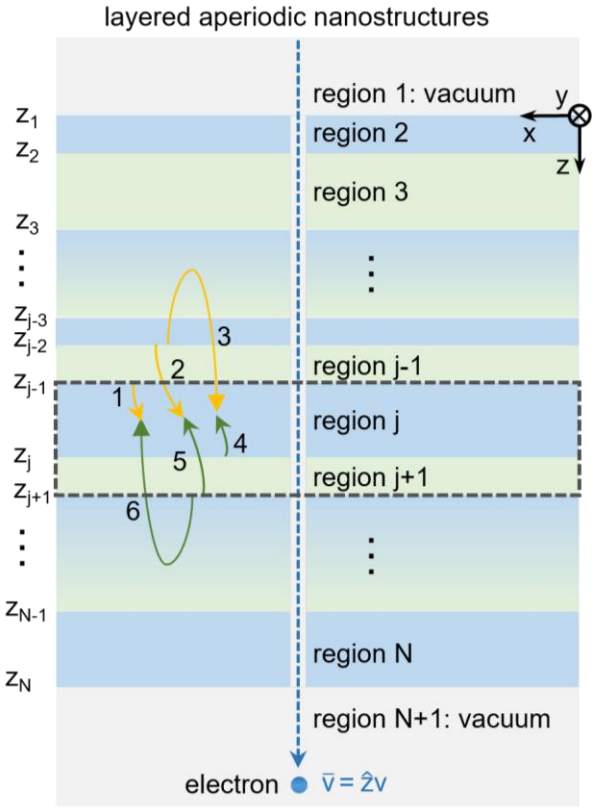

Fig. S2. Structural schematic of the interference of multiple transition radiation created at various optical interfaces.

Part 1: Field in region j from the forward transition radiation at the $j-1|j$ interface

From the viewpoint of geometric optics, the forward transition radiation at the $j-1|j$ interface contributing to the field in region j is

$$\begin{aligned} TR_j^+ \to Region\ j\ &= A_{j,0}^+ \cdot \left[e^{ik_{z,j}(z-z_{j-1})} + \tilde{R}_{j|j+1} e^{2ik_{z,j}(d_j-d_{j-1})} e^{-ik_{z,j}(z-z_{j-1})}\right] \\ A_{j,0}^+ &= \frac{iq}{\omega\varepsilon_0(2\pi)^3} \cdot a_{j-1|j}^+ \cdot M_j \\ M_j &= \frac{1}{1-\tilde{R}_{j|j+1}\tilde{R}_{j|j-1} e^{2ik_{z,j}(z_j-z_{j-1})}} \end{aligned} \tag{S7}$$

where M_j characterizes the multiple reflections in region j at the $j-1|j$ and $j|j+1$ interfaces, and we have $M_1 = M_{N+1} = 1$; $\tilde{R}_{j|j-1}$ and $\tilde{R}_{j|j+1}$ are the generalized reflection and transmission coefficients for TM waves at the $j-1|j$ and $j|j+1$ interfaces, respectively, and they can be obtained by using an iteration relationship, namely

$$\tilde{R}_{j|j+1} = R_{j|j+1} + \frac{T_{j|j+1}\tilde{R}_{j+1|j+2}T_{j+1|j}e^{2ik_{z,j+1}\left(z_{j+1}-z_j\right)}}{1-R_{j+1|j}\tilde{R}_{j+1|j+2}e^{2ik_{z,j+1}\left(z_{j+1}-z_j\right)}}$$
$$\tilde{R}_{j|j-1} = R_{j|j-1} + \frac{T_{j|j-1}\tilde{R}_{j-1|j-2}T_{j-1|j}e^{2ik_{z,j-1}\left(z_{j-1}-z_{j-2}\right)}}{1-R_{j-1|j}\tilde{R}_{j-1|j-2}e^{2ik_{z,j-1}\left(z_{j-1}-z_{j-2}\right)}} \quad \text{(S8).}$$

The subscript of $\tilde{R}_{j|j+1}$ and $\tilde{R}_{j|j-1}$ indicates that the TM plane wave is incident from region j (the first number) and transmitted to region $j+1$ or $j-1$ (the second number), respectively. Especially, one has $\tilde{R}_{N|N+1} = R_{N|N+1}$ and $\tilde{R}_{2|1} = R_{2|1}$. The reflection and transmission coefficient for the field E_z at interface $z = z_j$ from region j to region $j+1$ can be expressed as $T_{j\,|\,j+1} = T^{\mathrm{TM}}\frac{\varepsilon_{\mathrm{r},j}}{\varepsilon_{\mathrm{r},j+1}} = \frac{2\varepsilon_{\mathrm{r},j+1}k_{z,j}}{\varepsilon_{\mathrm{r},j+1}k_{z,j}+\varepsilon_{\mathrm{r},j}k_{z,j+1}}\cdot\frac{\varepsilon_{\mathrm{r},j}}{\varepsilon_{\mathrm{r},j+1}}$ and $R_{j\,|\,j+1} = R^{\mathrm{TM}} = \frac{\varepsilon_{\mathrm{r},j+1}k_{z,j}-\varepsilon_{\mathrm{r},j}k_{z,j+1}}{\varepsilon_{\mathrm{r},j+1}k_{z,j}+\varepsilon_{\mathrm{r},j}k_{z,j+1}}$, where R^{TM} and T^{TM} are the reflection and transmission coefficients defined for the magnetic field $H_{\perp}$.

Part 2: Field in region j from the forward transition radiation at the $m-1|m$ $(2 \le m \le j-1)$ interface

Only part of the forward transition radiation at the $m-1|m$ $(2 \le m \le j-1)$ interface would transmit into region j $(j > m)$. These transmitted fields in region j can be expressed as

$$TR_m^+ \to Region\ j = C_{m|j}^+\left[e^{ik_{z,j}(z-z_{m-1})} + \tilde{R}_{j|j+1}e^{2ik_{z,j}\left(z_j-z_{m-1}\right)}e^{-ik_{z,j}(z-z_{m-1})}\right] \quad \text{(S9)}$$

The only unknown quantity $C_{m|j}^+$ can be obtained by recursively matching boundary conditions from region m to region j. For example, at the $z = z_m$ interface, we have

$$C_{m|m+1}^+e^{ik_{z,m+1}(z_m-z_{m-1})} = A_{m,0}^+e^{ik_{z,m}(z_m-z_{m-1})}\cdot S_{m|m+1} \quad \text{(S10)}$$

$$S_{m|m+1} = \frac{T_{m|m+1}}{1-R_{m+1|m}\tilde{R}_{m+1|m+2}e^{i2k_{z,m+1}(z_{m+1}-z_m)}} \quad \text{(S11)}$$

Namely, the value of $C_{m|m+1}^+$ is determined by $A_{m,0}^+$ and the transmission at the $m|m+1$ interface. Following equation (S10), we have

$$\prod_{n=m}^{n=j-1} C_{m|n+1}^+e^{ik_{z,n+1}(z_n-z_{m-1})} = \prod_{n=m}^{n=j-1} C_{m|n}^+e^{ik_{z,n}(z_n-z_{m-1})}\cdot S_{n|n+1} \quad \text{(S12)}$$

Especially, $C_{m|m}^+ = A_{m,0}^+$. From equation (S12), one has

$$C_{m|j}^+e^{ik_{z,j}\left(z_{j-1}-z_{m-1}\right)} = \tilde{T}_{m|j}^{j>m}\cdot A_{m,0}^+ \quad \text{(S13)}$$

$$\tilde{T}_{m|j}^{j>m} = \prod_{n=m}^{n=j-1} S_{n|n+1}\,e^{ik_{z,n}(z_n-z_{n-1})} \quad \text{(S14)}$$

where $\tilde{T}_{m|j}^{j>m}$ can be treated as the generalized transmission coefficient from region m to region j.

Part 3: Field in region j from the backward transition radiation at the $m|m+1$ $(2 \le m \le j-1)$ interface

The emitted field in region m from the backward transition radiation at the $m|m+1$ interface is written as

$$\begin{aligned} TR_m^- \to Region\ m &= A_{m,o}^- \left[e^{-ik_{z,m}(z-z_m)} + \tilde{R}_{m|m-1} e^{ik_{z,m}(z-z_m)} \cdot e^{-2ik_{z,m}(z_{m-1}-z_m)} \right] \\ A_{m,o}^- &= \frac{iq}{\omega \varepsilon_0 (2\pi)^3} \cdot a_{m|m+1}^- \cdot M_m \end{aligned} \tag{S15}$$

where the backward radiation factor $a_{m|m+1}^-$ of $m|m+1$ interface can be obtained from equation (S4). Equivalently, the emitted field in region m can be transformed to

$$\begin{aligned} TR_m^- \to Region\ m &= B_{m,o}^- e^{-ik_{z,m}(z-z_m)} + BR_{m,o}^+ \left[e^{+ik_{z,m}(z-z_m)} + \tilde{R}_{m|m+1} e^{-ik_{z,m}(z-z_m)} e^{+2ik_{z,m}(z_m-z_m)} \right] \\ BR_{m,o}^+ &= B_{m,o}^- M_m \tilde{R}_{m|m-1} e^{-2ik_{z,m}(z_{m-1}-z_m)} \\ B_{m,o}^- &= \frac{A_{m,o}^-}{M_m} = \frac{iq}{\omega \varepsilon_0 (2\pi)^3} \cdot a_{m|m+1}^- \end{aligned} \tag{S16}$$

In the transformation above, the relation of $M_m = 1 + M_m \tilde{R}_{m|m+1} \tilde{R}_{m|m-1} e^{2ik_{z,m}(z_m - z_{m-1})}$ is used. In this subsection, we only need to consider the part relevant to $BR_{m,o}^+$ in equation (S16).

Similar to equation (S9), we can express the transmitted field into region j as

$$TR_m^- \to Region\ j = D_{m|j}^+ \left[e^{ik_{z,j}(z-z_m)} + \tilde{R}_{j|j+1} e^{2ik_{z,j}(z_j-z_m)} e^{-ik_{z,j}(z-z_m)} \right] \tag{S17}$$

The calculation procedure for the unknown factor $D_{m|j}^+$ is the same as that of $C_{m|j}^+$. After some algebra, we have

$$D_{m|j}^+ e^{ik_{z,j}(z_{j-1}-z_m)} = \tilde{T}_{m|j}^{j>m} BR_{m,o}^+ \cdot e^{ik_{z,m}(z_{m-1}-z_m)} \tag{S18}$$

where $\tilde{T}_{m|j}^{j>m}$ is determined by equation (S14).

Part 4: Field in region j from the backward transition radiation at the $j|j+1$ interface

This part of radiation has actually been tackled in equation (S15). Namely, the related field is written as

$$\begin{aligned} TR_j^- \to region\ j &= A_{j,o}^- \left[e^{-ik_{z,j}(z-z_j)} + \tilde{R}_{j|j-1} e^{+ik_{z,j}(z-z_j)} \cdot e^{-2ik_{z,j}(z_{j-1}-z_j)} \right] \\ A_{j,o}^- &= \frac{iq}{\omega \varepsilon_0 (2\pi)^3} \cdot a_{j|j+1}^{-,o} e^{i\frac{\omega}{v} z_j} \cdot M_j \end{aligned} \tag{S19}$$

Part 5: Field in region j from the backward transition radiation at the $m|m+1$ $(j+1 \le m \le N)$ interface

The field in region j $(j < m)$ can be expressed as

$$TR_m^- \to region\ j = D_{m|j}^- \left[e^{-ik_{z,j}(z-z_m)} + \tilde{R}_{j|j-1} e^{+ik_{z,j}(z-z_m)} e^{-2ik_{z,j}(z_{j-1}-z_m)} \right] \tag{S20}$$

For $j = m-1$ in equation (S20), namely at the $m-1|m$ interface with $z = z_{m-1}$, one has

$$D_{m|m-1}^- e^{-ik_{z,m-1}(z_{m-1}-z_m)} = A_{m,o}^- e^{-ik_{z,m}(z_{m-1}-z_m)} \cdot S_{m|m-1} \tag{S21}$$

$$S_{m|m-1} = \frac{T_{m|m-1}}{1 - R_{m-1|m}\tilde{R}_{m-1|m-2}e^{2ik_{z,m-1}(z_{m-1}-z_{m-2})}} \tag{S22}$$

where $D^-_{m|m-1}$ is determined by $A^-_{m,0}$ and the transmission at the $m-1|m$ interface. From equation (S21), one has

$$\prod_{n=j}^{n=m-1} D^-_{m|n}e^{-ik_{z,n}(z_n-z_m)} = \prod_{n=j}^{n=m-1} D^-_{m|n+1}e^{-ik_{z,n+1}(z_n-z_m)}S_{n+1|n} \tag{S23}$$

Especially, $D^-_{m|m} = A^-_{m,0}$. From equation (S23), the unknown parameter $D^-_{m|j}$ in equation (S20) can be determined by

$$D^-_{m|j}e^{-ik_{z,j}(z_j-z_m)} = \tilde{T}^{j<m}_{m|j} \cdot A^-_{m,o} \tag{S24}$$

$$\tilde{T}^{j<m}_{m|j} = \prod_{n=j}^{n=m-1} S_{n+1|n}\, e^{-ik_{z,n+1}(z_n-z_{n+1})} \tag{S25}$$

where $\tilde{T}^{j<m}_{m|j}$ can be treated as the generalized transmission coefficient from region m to region j ($m > j$).

Part 6: Field in region j from the forward transition radiation at the $m-1|m$ ($j+1 \le m \le N$) interface

By following equation (S8), the forward transition radiation emitted in region m can be transformed to

$$\begin{gathered} TR^+_m \to region\ m = B^+_{m,o}e^{ik_{z,m}(z-z_{m-1})} + AR^-_{m,o}\left[e^{-ik_{z,m}(z-z_{m-1})} + \tilde{R}_{m|m-1}e^{ik_{z,m}(z-z_{m-1})}\right] \\ AR^-_{m,o} = B^+_{m,o}M_m\tilde{R}_{m|m+1}e^{2ik_{z,m}(z_m-z_{m-1})} \\ B^+_{m,o} = \frac{A^+_{m,o}}{M_m} = \frac{iq}{\omega\varepsilon_0(2\pi)^3}\cdot a^+_{m-1|m} \end{gathered} \tag{S26}$$

Here we only need to take the part relevant to $AR^-_{m,o}$ in equation (S26) into consideration. In a multi-layered system, the transmitted field in region j ($j < m$) from the forward transition radiation at the $m-1|m$ ($j < m \le N-1$) can be written as

$$TR^+_m \to region\ j = C^-_{m|j}\left[e^{-ik_{z,j}(z-z_{m-1})} + \tilde{R}_{j|j-1}e^{+ik_{z,j}(z-z_{m-1})}e^{-2ik_{z,j}(z_{j-1}-z_{m-1})}\right] \tag{S27}$$

By performing similar procedure to part 5, we have

$$C^-_{m|j}e^{-ik_{z,j}(z_j-z_{m-1})} = \tilde{T}^{j<m}_{m|j} \cdot AR^-_{m,o}e^{-ik_{z,m}(z_m-z_{m-1})} \tag{S28}$$

where $\tilde{T}^{j<m}_{m|j}$ is determined by equation (S25).

Part 7: Interference of transition radiation from multiple parallel interfaces

The total electric field in region j ($1 \le j \le N+1$) can now be expressed as

$$E_{z,j}^{R}=\begin{cases}\dfrac{iq}{\omega\varepsilon_0(2\pi)^3}\cdot a_1\cdot e^{-ik_{z,1}(z-z_1)} & (j=1)\\ \dfrac{iq}{\omega\varepsilon_0(2\pi)^3}\left[a_j^{-}\cdot e^{-ik_{z,j}(z-z_j)}+a_j^{+}\cdot e^{ik_{z,j}(z-z_{j-1})}\right] & (2\le j\le N)\\ \dfrac{iq}{\omega\varepsilon_0(2\pi)^3}\cdot a_{N+1}\cdot e^{ik_{z,N+1}(z-z_N)} & (j=N+1)\end{cases} \tag{S29}$$

where a_j^{+} (a_j^{-}) represents the generalized forward (backward) radiation factor in region j and can be determined by the derivations in parts 1-6.

As an example, the radiation in region $N+1$ originates solely from all the interfaces above region j ($j=N+1$)

$$TR_j^{+}\rightarrow Region\ j+\sum_{m=2}^{j-1}TR_m^{+}\rightarrow Region\ j+\sum_{m=2}^{j-1}TR_m^{-}\rightarrow Region\ j \tag{S30}$$

where the components in equation (S30) are determined by equations (S7,S9,S15) as elaborated in detail in parts 1-3. To be specific, when $j=N+1$, no backward-propagating field is generated, i.e. $a_{N+1}^{-}=0$. Therefore, by comparing equations (S29,S30), the radiation factor a_{N+1}^{+} can be expressed as

$$a_{N+1}^{+}=\frac{\omega\varepsilon_0(2\pi)^3}{iq}\cdot\left[A_{N+1,0}^{+}+\sum_{m=2}^{N}\left(C_{m|N+1}^{+}e^{ik_{z,N+1}(z_N-z_{m-1})}+D_{m|N+1}^{+}e^{ik_{z,N+1}(z_N-z_m)}\right)\right] \tag{S31}$$

With the aid of equations (S13,S18), we further obtain

$$a_{N+1}^{+}=\frac{\omega\varepsilon_0(2\pi)^3}{iq}\cdot\left[A_{N+1,0}^{+}+\sum_{m=2}^{N}\left(\tilde{T}_{m|N+1}^{N+1>m}\cdot A_{m,0}^{+}+\tilde{T}_{m|N+1}^{N+1>m}\cdot BR_{m,o}^{+}e^{ik_{z,m}(z_{m-1}-z_m)}\right)\right] \tag{S32}$$

S1.3 Angular spectral energy density of resonance transition radiation

In this subsection we calculate the forward angular spectral energy density of resonance transition radiation $U(\lambda,\theta)$. Note that we leave out the subscript F in U_{F} in the following and the main text, since we only discuss the forward radiation in the main text. $U(\lambda,\theta)$ is defined by

$$W=\int_0^{+\infty}d\omega\int_0^{\frac{\pi}{2}}d\theta\ U(\lambda,\theta)\cdot(2\pi\sin\theta) \tag{S33}$$

where the radiation angle θ is the angle made by the wavevector $\bar{k}$ and $\bar{v}$, and W is the the energy of the radiation field $\bar{E}_{N+1}^{R}$ in region $N+1$. It's sufficient to calculate the energy of the radiation field E^R asympthotically as $t\rightarrow\infty$, at which the radiated wave train is already at a great distance to the interface and then E^R is separated from the charge field E^q. This way,

$$W = \varepsilon_{N+1}\lim_{t\to\infty}\int d\bar{r}|\,\bar{E}^R_{N+1}(\bar{r},t)|^2 = \varepsilon_1\lim_{t\to\infty}\int d\bar{r}_\perp\int_{-\infty}^{\infty}dz\,|\,\bar{E}^R_{N+1}(\bar{r},t)|^2 \tag{S34}$$

$$|\bar{E}^R_{N+1}(\bar{r},t)|^2 = \int d\bar{k}_\perp d\bar{k}'_\perp d\omega d\omega' \bar{E}^R_{\bar{k}_\perp,\omega,N+1}(z)\bar{E}^R_{\bar{k}'_\perp,\omega',N+1}{}^*(z)e^{i[(\bar{k}_\perp-\bar{k}'_\perp)\cdot\bar{r}_\perp-(\omega-\omega')t]} \tag{S35}$$

By substituting equation (S35) into (S34) and integrating over $d\bar{r}_\perp dz d\bar{k}'_\perp d\omega'$ in equation (S35), one has

$$W = 2\int_0^{+\infty}\int \varepsilon_{N+1}|a_{N+1}|^2\left(\frac{q}{\omega\varepsilon_0(2\pi)^3}\right)^2\frac{\omega^2\sqrt{\varepsilon_{\mathrm{r},N+1}}}{ck_\perp^2}\sqrt{1-\frac{k_\perp^2c^2}{\omega^2\varepsilon_{\mathrm{r},N+1}}}(2\pi)^3\,d\bar{k}_\perp d\omega \tag{S36}$$

For all emitted photons, the integration over $d\bar{k}_\perp$ should be taken under the condition of $k_\perp^2 \le \frac{\omega^2}{c^2}\varepsilon_{\mathrm{r},N+1}$.

From equations (S33,S36), one has

$$U(\lambda,\theta) = \frac{\varepsilon_{\mathrm{r},N+1}^{3/2}q^2\cos^2\theta\,|a_{N+1}|^2}{4\pi^3\varepsilon_0 c\sin^2\theta} \tag{S37}$$

S1.4 Field distribution of excited resonance transition radiation

By following the same procedure as equation (S6), the field distribution can be written as

$$\begin{gathered}\bar{E}_z(\bar{r},t) = \bar{E}_z^q(\bar{r},t) + \bar{E}_z^R(\bar{r},t)\\ \bar{E}^q_{z,j}(\bar{r},t) = \hat{z}\int_{-\infty}^{\infty}d\omega\frac{-q}{8\pi\omega\varepsilon_0\varepsilon_{\mathrm{r},j}}\left(\frac{\omega^2}{c^2}\varepsilon_{\mathrm{r},j}-\frac{\omega^2}{v^2}\right)H_0^{(1)}\left(\rho\sqrt{\frac{\omega^2}{c^2}\varepsilon_{\mathrm{r},j}-\frac{\omega^2}{v^2}}\right)e^{i\frac{\omega}{v}z-\omega t}\\ \bar{E}^R_{z,j}(\bar{r},t) = \hat{z}\int_{-\infty}^{\infty}d\omega\int_0^{\infty}dk_\perp\frac{iq}{\omega\varepsilon_0(2\pi)^3}\left(2\pi k_\perp J_0(k_\perp\rho)\right)\left[a_j^-e^{-ik_{z,j}(z-z_j)-i\omega t}+a_j^+e^{ik_{z,j}(z-z_{j-1})-i\omega t}\right]\end{gathered} \tag{S38}$$

where the only unknown radiation factors a_j^- and a_j^+ can be determined in part 7 of the section 1.3.

Section S2: Resonance transition radiation via Brewster randomness at the Brewster angle

S2.1 Dependence of $U(\lambda_0,\theta_{\mathrm{B,vac}})$ on the interface number

In this subsection, we analyze the dependence of $U(\lambda_0,\theta_{\mathrm{B,vac}})$ on the interface number.

For Fig. 3 in the main text, there is zero reflection at the first and the last interfaces, namely $R_{2|1}=0$ and $R_{N|N+1}=0$. By following equation (S8), one has

$$\tilde{R}_{j+1|j} = \tilde{R}_{j|j+1} = 0, \forall j = 1,2,\dots N \tag{S39}$$

Therefore, one has $A^+_{N+1,0} = \frac{iq}{\omega\varepsilon_0(2\pi)^3}a^+_{N|N+1}$, $A^+_{m,0} = \frac{iq}{\omega\varepsilon_0(2\pi)^3}a^+_{m-1|m}$, $BR^+_{m,o}=0$ and $\tilde{T}^{N+1>m}_{m|N+1} = \prod_{n=m}^{n=N}T_{n|n+1}e^{ik_{z,n}(z_n-z_{n-1})}$. Substituting these into equation (S32), one has

$$
\begin{aligned}
a_{N+1}^{+} &= \frac{\omega\varepsilon_0(2\pi)^3}{iq}\cdot\left[A_{N+1,0}^{+}+\sum_{m=2}^{N}\left(\tilde{T}_{m|N+1}^{N+1>m}\cdot A_{m,0}^{+}+\tilde{T}_{m|N+1}^{N+1>m}\cdot BR_{m,o}^{+}e^{ik_{z,m}(z_{m-1}-z_m)}\right)\right] \\
&= a_{N|N+1}^{+}+\sum_{m=2}^{N}\left(\prod_{n=m}^{n=N}T_{n|n+1}e^{ik_{z,n}(d_n-d_{n-1})}\cdot a_{m-1|m}^{+}\right)
\end{aligned}
\tag{S40}
$$

Based on the phase coherence condition of $k_{z,n}d_{\mathrm{X}}=\frac{\omega}{v}d_{\mathrm{X}}-(2m_{\mathrm{X}}+1)\pi$, where $d_{\mathrm{X}}=z_j-z_{j-1}$ is the thickness of the corresponding layer composed of dielectric X, and $m_{\mathrm{X}}\geq 0$ is a random integer. One has

$$
\begin{aligned}
a_{N+1}^{+} &= a_{N|N+1}^{+}+\sum_{m=2}^{N}\left(\prod_{n=m}^{n=N}T_{n|n+1}e^{i\left[\frac{\omega}{v}(z_n-z_{n-1})-(2m+1)\pi\right]}\cdot a_{m-1|m}^{+}\right) \\
&= a_{N|N+1}^{+}+\sum_{m=2}^{N}\left((-1)^{N-m+1}e^{i\frac{\omega}{v}(z_N-z_{m-1})}\cdot a_{m-1|m}^{+}\prod_{n=m}^{n=N}T_{n|n+1}\right) \\
&= e^{i\frac{\omega}{v}d_N}\left\{a_{N|N+1}^{+,0}+\sum_{m=2}^{N}\left[(-1)^{N-m+1}a_{m-1|m}^{+}e^{-i\frac{\omega}{v}d_{m-1}}\frac{\varepsilon_{\mathrm{r},m}}{\varepsilon_{\mathrm{r},N}}T_{N|N+1}\right]\right\} \\
&= e^{i\frac{\omega}{v}d_N}\left\{a_{N|N+1}^{+,0}+T_{N|N+1}\sum_{m=2}^{N}\left[(-1)^{N-m+1}a_{m-1|m}^{+,0}\frac{\varepsilon_{\mathrm{r},m}}{\varepsilon_{\mathrm{r},N}}\right]\right\}
\end{aligned}
\tag{S41}
$$

If medium II is set as air, one has

$$
a_{N+1}^{+}=\frac{e^{i\frac{\omega}{v}z_N}N}{2}\left(-a_{1|2}^{+,0}\varepsilon_{\mathrm{r},2}+a_{2|3}^{+,0}\right) \tag{S42}
$$

Substituting equation (S42) into (S37), one can easily obtain the angular energy density at Brewster angle as

$$
\begin{aligned}
U\left(\lambda_0,\theta_{\mathrm{B,vac}}\right) &= \frac{q^2\cos^2\theta_{\mathrm{B,vac}}\left|a_{N+1}\right|^2}{4\pi^3\varepsilon_0 c\sin^2\theta_{\mathrm{B,vac}}}=\frac{q^2\cos^2\theta_{\mathrm{B,vac}}}{4\pi^3\varepsilon_0 c\sin^2\theta_{\mathrm{B,vac}}}\left|\frac{e^{i\frac{\omega}{v}d_N}N}{2}\left(a_{\mathrm{II|I}}^{+,0}\varepsilon_{\mathrm{r,I}}-a_{\mathrm{I|II}}^{+,0}\right)\right|^2 \\
&= \frac{q^2N^2}{16\pi^3\varepsilon_0 c}\cdot\frac{\varepsilon_{\mathrm{r,II}}}{\varepsilon_{\mathrm{r,I}}}\left|\left(a_{\mathrm{II|I}}^{+,0}\varepsilon_{\mathrm{r,I}}-a_{\mathrm{I|II}}^{+,0}\right)\right|^2=\frac{q^2N^2}{16\pi^3\varepsilon_0 c}\left|\left(a_{\mathrm{II|I}}^{+,0}\varepsilon_{\mathrm{r,I}}-a_{\mathrm{I|II}}^{+,0}\right)\right|^2
\end{aligned}
\tag{S43}
$$

where the identities $\varepsilon_{\mathrm{r,II}}=\varepsilon_{\mathrm{r},N+1}=1$, $\sin\theta_{\mathrm{B,vac}}=\sqrt{\frac{\varepsilon_{\mathrm{r,I}}\varepsilon_{\mathrm{r,II}}}{\varepsilon_{\mathrm{r,I}}+\varepsilon_{\mathrm{r,II}}}}$ and $\cos\theta_{\mathrm{B,vac}}=\frac{\varepsilon_{\mathrm{r,II}}}{\sqrt{\varepsilon_{\mathrm{r,I}}+\varepsilon_{\mathrm{r,II}}}}$ are used.

From equation (S43), if the electron velocity and constituent media are fixed, $U\left(\lambda_0,\theta_{\mathrm{B,vac}}\right)$ is a constant, and is it proportional to the interface number squared.

S2.2 Dependence of $U\left(\lambda_0,\theta_{\mathrm{B,vac}}\right)$ on the dielectric permittivities and the electron velocity

In this subsection, we analyze the dependence of radiation intensity on permittivities and the electron velocity. From equation (S5), one has

$$a_{\mathrm{I|II}}^{+,0}=\frac{\frac{v}{c}\cdot\frac{k_{\perp}^{2}c^{2}}{\omega^{2}}}{\left(\varepsilon_{\mathrm{r,I}}\frac{k_{z,\mathrm{II}}}{\omega/c}+\varepsilon_{\mathrm{r,II}}\frac{k_{z,\mathrm{I}}}{\omega/c}\right)}\cdot\left[\frac{1+\frac{v}{c}\cdot\frac{k_{z,\mathrm{I}}}{\omega/c}}{\left(1-\frac{v^{2}}{c^{2}}\varepsilon_{\mathrm{r,I}}+\frac{k_{\perp}^{2}v^{2}}{\omega^{2}}\right)}-\frac{\frac{\varepsilon_{\mathrm{r,I}}}{\varepsilon_{\mathrm{r,II}}}+\frac{v}{c}\cdot\frac{k_{z,\mathrm{I}}}{\omega/c}}{\left(1-\frac{v^{2}}{c^{2}}\varepsilon_{\mathrm{r,II}}+\frac{k_{\perp}^{2}v^{2}}{\omega^{2}}\right)}\right]$$
$$a_{\mathrm{II|I}}^{+,0}=\frac{-\frac{v}{c}\cdot\frac{k_{\perp}^{2}c^{2}}{\omega^{2}}}{\left(\varepsilon_{\mathrm{r,II}}\frac{k_{z,\mathrm{I}}}{\omega/c}+\varepsilon_{\mathrm{r,I}}\frac{k_{z,\mathrm{II}}}{\omega/c}\right)}\cdot\left[\frac{1+\frac{v}{c}\cdot\frac{k_{z,\mathrm{II}}}{\omega/c}}{\left(1-\frac{v^{2}}{c^{2}}\varepsilon_{\mathrm{r,II}}+\frac{k_{\perp}^{2}v^{2}}{\omega^{2}}\right)}-\frac{\frac{\varepsilon_{\mathrm{r,II}}}{\varepsilon_{\mathrm{r,I}}}+\frac{v}{c}\cdot\frac{k_{z,\mathrm{II}}}{\omega/c}}{\left(1-\frac{v^{2}}{c^{2}}\varepsilon_{\mathrm{r,I}}+\frac{k_{\perp}^{2}v^{2}}{\omega^{2}}\right)}\right] \quad \text{(S44)}$$

At the Brewster angle, substituting $\frac{\varepsilon_{\mathrm{r,II}}}{\varepsilon_{\mathrm{r,I}}}=\frac{k_{z,\mathrm{II}}}{k_{z,\mathrm{I}}}$ into equation (S44), one has

$$a_{\mathrm{I|II}}^{+,0}=-a_{\mathrm{II|I}}^{+,0}\frac{\varepsilon_{\mathrm{r,I}}}{\varepsilon_{\mathrm{r,II}}} \quad \text{(S45)}$$

Equation (S45) can be re-organized as

$$a_{\mathrm{I|II}}^{+,0}=-a_{\mathrm{II|I}}^{+,0}T_{\mathrm{I|II}} \quad \text{(S46)}$$

where $T_{\mathrm{I|II}}=\frac{\varepsilon_{\mathrm{r,I}}}{\varepsilon_{\mathrm{r,II}}}$ is transmission coefficient for E_z field of *p*-polarized wave at the Brewster angle. By substituting equation (S45) into (S43), one has

$$U\left(\lambda_0,\theta_{\mathrm{B,vac}}\right)=\frac{q^{2}N^{2}}{4\pi^{3}\varepsilon_{0}c\varepsilon_{\mathrm{r,I}}}\left|a_{\mathrm{I|II}}^{+,0}\right|^{2} \quad \text{(S47)}$$

where $a_{\mathrm{I|II}}^{+,0}$ is a function of permittivity and electron velocity, and can be simplified from equation (S44) as

$$a_{\mathrm{I|II}}^{+,0}=\frac{-\frac{v}{c}\cdot\left(\varepsilon_{\mathrm{r,I}}-1\right)\left(1-\frac{v^{2}}{c^{2}}-\frac{v}{c}\cdot\frac{\varepsilon_{\mathrm{r,I}}}{\sqrt{\varepsilon_{\mathrm{r,I}}+1}}\right)}{2\sqrt{\varepsilon_{\mathrm{r,I}}+1}\left(1-\frac{v^{2}}{c^{2}}\frac{1}{\varepsilon_{\mathrm{r,I}}+1}\right)\left(1-\frac{v}{c}\cdot\frac{\varepsilon_{\mathrm{r,I}}}{\sqrt{\varepsilon_{\mathrm{r,I}}+1}}\right)} \quad \text{(S48)}$$

Critically, equation (S48) represents that the design of a multilayer aperiodic nanostructure with Brewster randomness could be readily reduced to the scenario for a single optical interface.

Section S3: Influence of short-range disorders on the performance of Brewster randomness

S3.1 Comparison for the long-range Brewster randomness and short-range structural disorders

In this subsection, we compare the long-range Brewster randomness and the short-range structural disorders, as described by a discrete random variable $p(m_{\mathrm{X}})$ and a continuous random variable $f(\Delta)$ respectively, where $\Delta=d_{\mathrm{X}}-(2m_{\mathrm{X}}+1)d_{\mathrm{B,X}}$. The layer thickness follows a probability distribution function of $P(d_{\mathrm{X}})=p(m_{\mathrm{X}})f(\Delta)$. On the Brewster randomness side, $p(m_{\mathrm{X}})$ could be any discrete random distribution [7], such as the decimal expansion of π shown in Fig. 3*A*. On the other structural disorder side, $f(\Delta)$ could take the form of the uniform and exponential distribution [8,9] in Fig. S3*B*, which are respectively determined by

$$f(\Delta) = \frac{1}{\Delta_0}, \quad \text{when } |\Delta| < \Delta_0 \tag{S49}$$

$$f(\Delta) = \frac{1}{\Delta} e^{-\frac{\Delta_0}{\Delta}}, \quad \text{when } \Delta > 0 \tag{S50}$$

where Δ_0 represents different degrees of the structural disorder. If there is no structural disorder from sample fabrication, namely $\Delta_0 \to 0$, $f(\Delta)$ is equivalent to the delta function $\delta(\Delta)$, which is used in the main text.

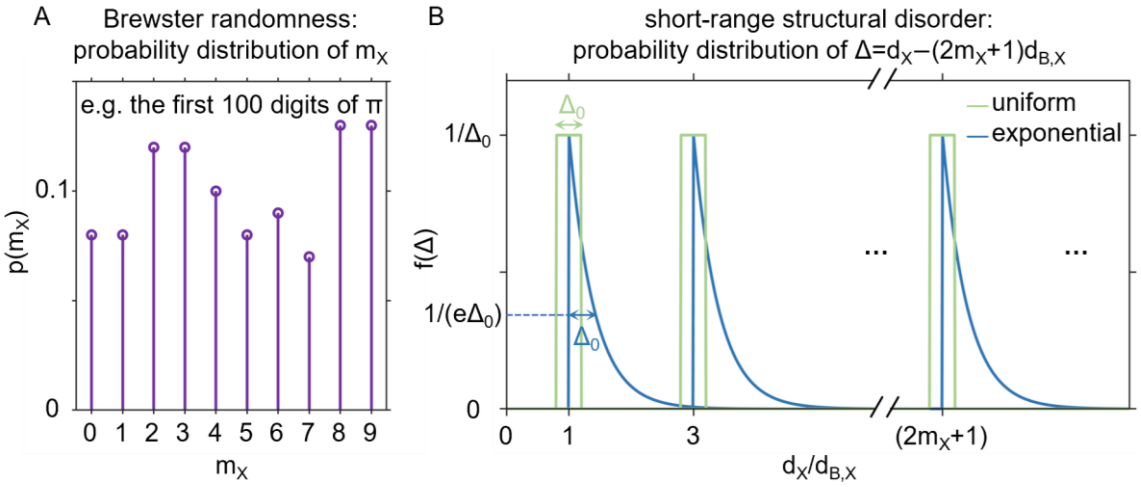

Fig. S3. Probability distribution of layer thickness near $d_{\mathrm{X}} = (2m_{\mathrm{X}} + 1)d_{\mathrm{B,X}}$ for layered aperiodic multilayers with both the Brewster randomness and structural disorder. (*A*) Brewster randomness represented by $p(m_{\mathrm{X}})$. (*B*) Structural disorder represented by $f(\Delta)$, which typically originates from sample fabrication.

S3.2 Influence of short-range structural disorders

In this subsection, we show the influence of short-range structural disorder from sample fabrication on resonance transition radiation via Brewster randomness. In Fig. S4, we show resonance transition radiation via Brewster randomness in presence of structural disorder governed by different kinds of probability distributions. Consistent with the conclusion drawn in main text, resonance transition radiation via Brewster randomness could arise only if $d_{0,\mathrm{I}}/d_{\mathrm{B,I}}$ is an odd integer. Further in Fig. S5, we show resonance transition radiation via Brewster randomness has a certain degree of tolerance to structural disorder, by introducing different degrees of structural disorder.

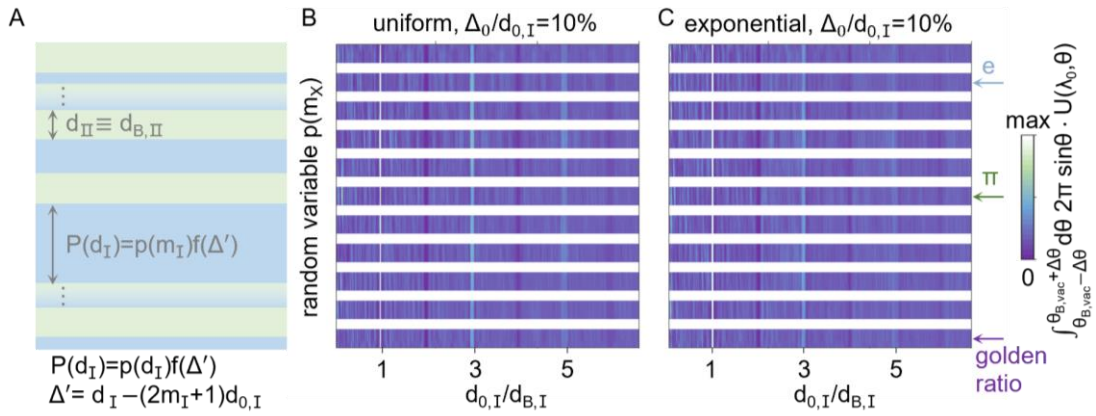

Fig. S4. Resonance transition radiation via Brewster randomness in presence of short-range structural disorder governed by different probability distributions. (*A*) Structural schematic. The setup here is the same as Fig. 2 in the main text, except that structural disorder described by $f(\Delta')$ is introduced in the layers consisting of dielectric I, where $\Delta' = d_{\mathrm{I}} - (2m_{\mathrm{I}} + 1)d_{0,\mathrm{I}}$. (*B* and *C*) $\int_{\theta_{\mathrm{B,vac}}-\Delta\theta}^{\theta_{\mathrm{B,vac}}+\Delta\theta} d\theta(2\pi \sin\theta)U(\lambda_0,\theta)$ as a function of $d_{0,\mathrm{I}}$ for various random variables $p(m_{\mathrm{X}})$. In *B* and *C*, $f(\Delta')$ is the uniform and exponential distribution in equations (S49-S50), respectively. Here, $\Delta_0/d_{0,\mathrm{I}} = 10\%$ is used.

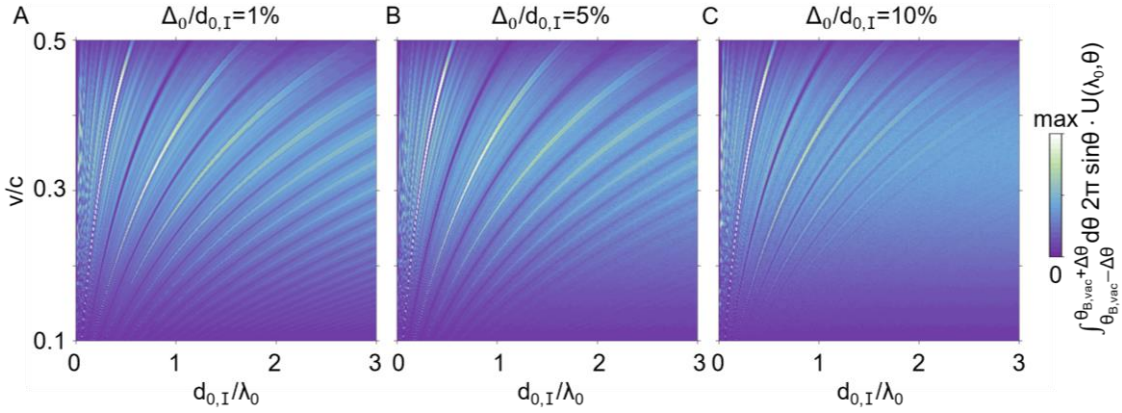

Fig. S5. Resonance transition radiation via Brewster randomness under different degrees of structural disorder. The setup is the same as Figure S4. (*A-C*) $\int_{\theta_{\mathrm{B,vac}}-\Delta\theta}^{\theta_{\mathrm{B,vac}}+\Delta\theta} d\theta(2\pi \sin\theta)U(\lambda_0,\theta)$ as a function of $d_{0,\mathrm{I}}$ and v with the random integer $m_{\mathrm{I}} \in [0,9]$. The variations in the thickness of layer composed of dielectric I follows the uniform distribution in equation (S49), and $\Delta_0/d_{0,\mathrm{I}}$ is 1%, 5% and 10% in *A-C*, respectively.

Section S4: More discussion on resonance transition radiation via Brewster randomness

S4.1 Destructive interference of multiple transition radiation created at adjacent interfaces

In this subsection, we demonstrate the destructive interference of multiple transition radiation created at adjacent interfaces. In principle, the multiple transition radiation created at adjacent interfaces could be

engineered to interfere either constructively or destructively at the Brewster angle on demand. To be specific, if the phase difference $\Delta\varphi = \varphi_j - \varphi_{j-1}$ between the multiple transition radiation at adjacent interfaces is an even multiple of π in Fig. S6*A*, namely $\Delta\varphi = 2m_{\mathrm{X}} \cdot \pi$ (m_{X} is an integer), these multiple transition radiation would interfere constructively, leading to the emergence of radiation peaks in Fig. S6*C* and Fig. 2 *C* and *D*. Based on the ray optics, when $\Delta\varphi = 2m_{\mathrm{X}} \cdot \pi$, we have $d_{\mathrm{X}}/d_{\mathrm{B,X}} = 2m_{\mathrm{X}} + 1$, namely that $d_{\mathrm{X}}/d_{\mathrm{B,X}}$ is an odd integer. By contrast, if $\Delta\varphi$ is an odd multiple of π in Fig. S6*B*, namely $\Delta\varphi = (2m_{\mathrm{X}} - 1) \cdot \pi$, these multiple transition radiation would interfere destructively, giving rise to the radiation dips in Fig. S6 *C* and Fig. 2 *C* and *D*. According to the ray optics, we have $d_{\mathrm{X}}/d_{\mathrm{B,X}} = 2m_{\mathrm{X}}$, namely that $d_{\mathrm{X}}/d_{\mathrm{B,X}}$ is an even integer, if $\Delta\varphi = (2m_{\mathrm{X}} - 1) \cdot \pi$.

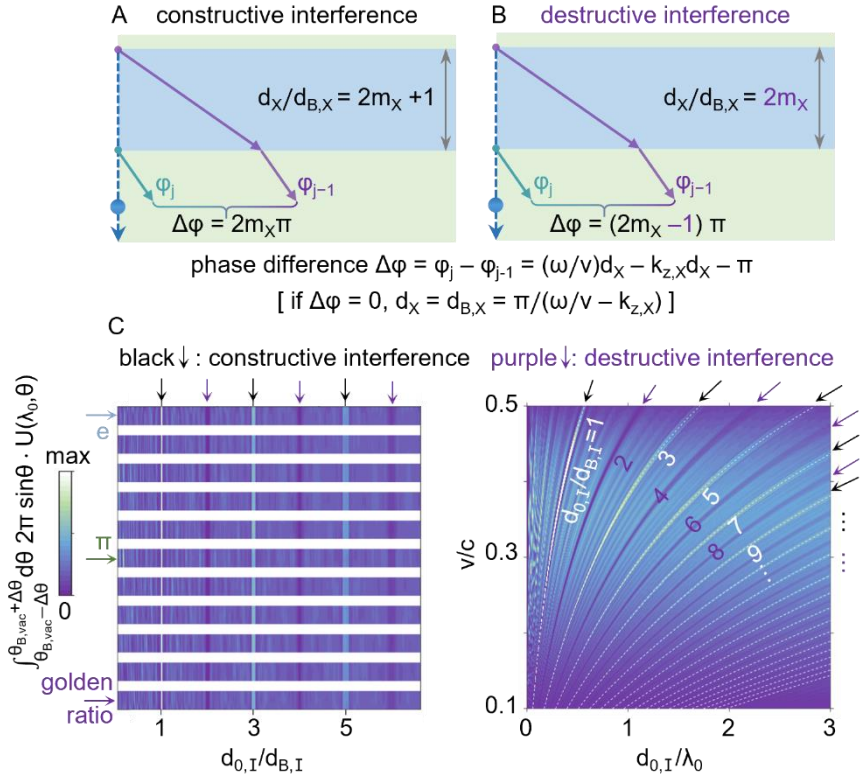

Fig. S6. Conceptual illustration of constructive and destructive interference of multiple transition radiation created at adjacent interfaces. The structural setup is the same as Fig. 2 in the main text. (*A* and *B*) Illustration of the phase difference $\Delta\varphi$ between transition radiation created at adjacent interfaces and layer thickness required for the constructive and destructive interference. (*C*) Left panel: $\int_{\theta_{\mathrm{B,vac}}-\Delta\theta}^{\theta_{\mathrm{B,vac}}+\Delta\theta} d\theta(2\pi \sin\theta)U(\lambda_0,\theta)$ as a function of $d_{0,\mathrm{I}}$ for various randomness, under the scenario of $v = v_0 = 0.3c$ and $\Delta\theta = 5°$. Right panel: $\int_{\theta_{\mathrm{B,vac}}-\Delta\theta}^{\theta_{\mathrm{B,vac}}+\Delta\theta} d\theta(2\pi \sin\theta)U(\lambda_0,\theta)$ as a function of $d_{0,\mathrm{I}}$ and v, with computer-generated random integer $m_{\mathrm{I}} \in$

[0,9]. When $d_{\mathrm{X}}/d_{\mathrm{B,X}}$ is an odd integer (i.e. $d_{\mathrm{X}}/d_{\mathrm{B,X}} = 2m_{\mathrm{X}} + 1$), the phase difference $\Delta\varphi$ is an even multiple of π (i.e. $\Delta\varphi = 2m_{\mathrm{X}} \cdot \pi$), resulting in the constructive interference in (*A*) and the emergence of radiation peaks (see black arrows) in (*C*), where m_{X} is an integer. By contrast, when $d_{\mathrm{X}}/d_{\mathrm{B,X}}$ is an even integer (i.e. $d_{\mathrm{X}}/d_{\mathrm{B,X}} = 2m_{\mathrm{X}}$), the phase difference $\Delta\varphi$ is an odd multiple of π (i.e. $\Delta\varphi = (2m_{\mathrm{X}} - 1) \cdot \pi$), resulting in the destructive interference in (*B*) and the emergence of radiation dips (see purple arrows) in (*C*).

S4.2 Influence of the material dispersion

In this subsection, we show the influence of the material dispersion on resonance transition radiation via Brewster randomness.

(a) Robustness of resonance transition radiation via Brewster randomness to the wavelength

Strictly speaking, only the radiation peak at the special point $(\theta_{\mathrm{B,vac}}, \lambda_0)$ of the energy-momentum space of emitted light in Fig. 3*A*-*C* is invariant to the variations of Brewster randomness. When $\lambda \to \lambda_0$ and $\theta \to \theta_{\mathrm{B,vac}}$, there is also the appearance of a bunch of radiation peaks, which are relatively insensitive to the variation of Brewster randomness. This phenomenon essentially indicates that our revealed resonance transition radiation via Brewster randomness is to some degree robust to the wavelength λ of light. Upon close inspection, the occurrence of this phenomenon is closely related to the phase coherence condition of $\mathrm{mod}(\Delta\varphi, 2\pi) = 0$. According to this phase coherence condition, the corresponding layer thickness is obtained as $d_{\mathrm{X}} = (2m_{\mathrm{X}} + 1)d_{\mathrm{B,X}}$ and $d_{\mathrm{B,X}} = \lambda/\left[2\left(c/v - \varepsilon_{\mathrm{r,X}}/\sqrt{\varepsilon_{\mathrm{r,I}} + \varepsilon_{\mathrm{r,II}}}\right)\right]$ (i.e. equations (2-3) in the main text). Since the Brewster angle in vacuum has $\sin\theta_{\mathrm{B,vac}} = \sqrt{\varepsilon_{\mathrm{r,I}}\varepsilon_{\mathrm{r,II}}/(\varepsilon_{\mathrm{r,I}} + \varepsilon_{\mathrm{r,II}})}$, the expression of $d_{\mathrm{B,X}}$ can be rewritten as

$$d_{\mathrm{B,X}} = \frac{\lambda}{2\left(c/v - \sqrt{\varepsilon_{\mathrm{r,X}} - \sin^2\theta_{\mathrm{B,vac}}}\right)} \tag{S51}$$

When there is no material dispersion, both $\varepsilon_{\mathrm{r,X}}$ and $\theta_{\mathrm{B,vac}}$ in equation (S51) are constants. This way, $d_{\mathrm{B,X}}$ is also a constant at a given working wavelength $\lambda = \lambda_0$. When $d_{\mathrm{B,X}}$ is fixed and the wavelength λ slightly deviates from the working wavelength λ_0 (i.e. $\lambda \neq \lambda_0$ but $\lambda \to \lambda_0$), equation (S51) can also be fulfilled if the radiation angle θ slightly deviates from the Brewster angle $\theta_{\mathrm{B,vac}}$ (i.e. $\theta \neq \theta_{\mathrm{B,vac}}$ but $\theta \to \theta_{\mathrm{B,vac}}$). This is exactly the fundamental reason for the emergence of a bunch of radiation peaks close to the special point of $(\theta_{\mathrm{B,vac}}, \lambda_0)$ in Fig. 3*A*-*C*. By following this thought, we further show in Fig. S7 that the emergence range for these radiation peaks in the energy-momentum space of emitted light can be flexibly engineered via the

manipulation of material dispersion. Briefly speaking, as the material dispersion increases, the emergence range for these radiation peaks would become narrower.

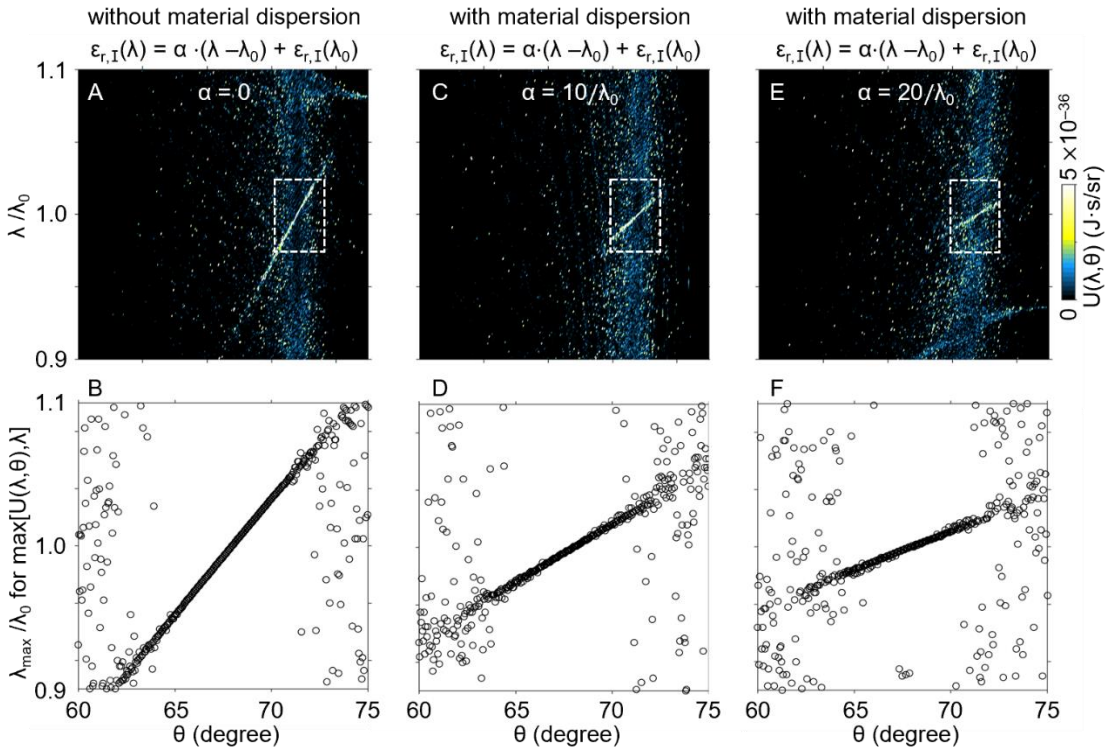

Fig. S7. Influence of the material dispersion on the robustness of the revealed resonance transition radiation via Brewster randomness to the wavelength. For illustration, we set $\varepsilon_{\mathrm{r,I}}(\lambda) = \alpha(\lambda - \lambda_0) + \varepsilon_{\mathrm{r,I}}(\lambda_0)$, where α is a self-defined parameter to characterize the material dispersion and λ_0 is the predefined working wavelength in vacuum. The other setup is the same as that in Fig. 3*C* of the main text. (*A* and *B*) $\alpha = 0$. That is, there is no material dispersion in the designed structure. (*C* and *D*) $\alpha = 10/\lambda_0$. (*E* and *F*) $\alpha = 20/\lambda_0$. To aid understanding, we show the angular spectral energy density $U(\lambda, \theta)$ of forward radiation from layered aperiodic nanostructures in (*A*, *C* and *E*). Meanwhile, the dependence of $\lambda_{\max}$ on θ is shown in (*B*, *D* and *F*), which is extracted from the regions highlighted by dashed white boxes in (*A*, *C* and *E*), respectively, based on the definition of $U(\lambda_{\max}, \theta) = \max[U(\lambda, \theta), \lambda]$.

(b) Influence of the material dispersion on resonance transition radiation via Brewster randomness

Furthermore, we show in Fig. S8 that when the interface number is finite (e.g. $N = 1000$), the intensity and directionality of the radiation peak at the special point $(\theta_{\mathrm{B,vac}}, \lambda_0)$ would not be affected by the material dispersion, as long as the properties of material remains unchanged at the predefined working wavelength $\lambda = \lambda_0$. The underlying reason is that our revealed phenomenon of resonance transition radiation via Brewster randomness is established on a single predefined working wavelength λ_0 and thus is irrelevant to

the material dispersion. In addition, when considering the influence of material loss, we will show in Fig. S9 that our revealed phenomenon of resonance transition radiation via Brewster randomness will remain almost unchanged when both the material loss and the interface number are reasonably large.

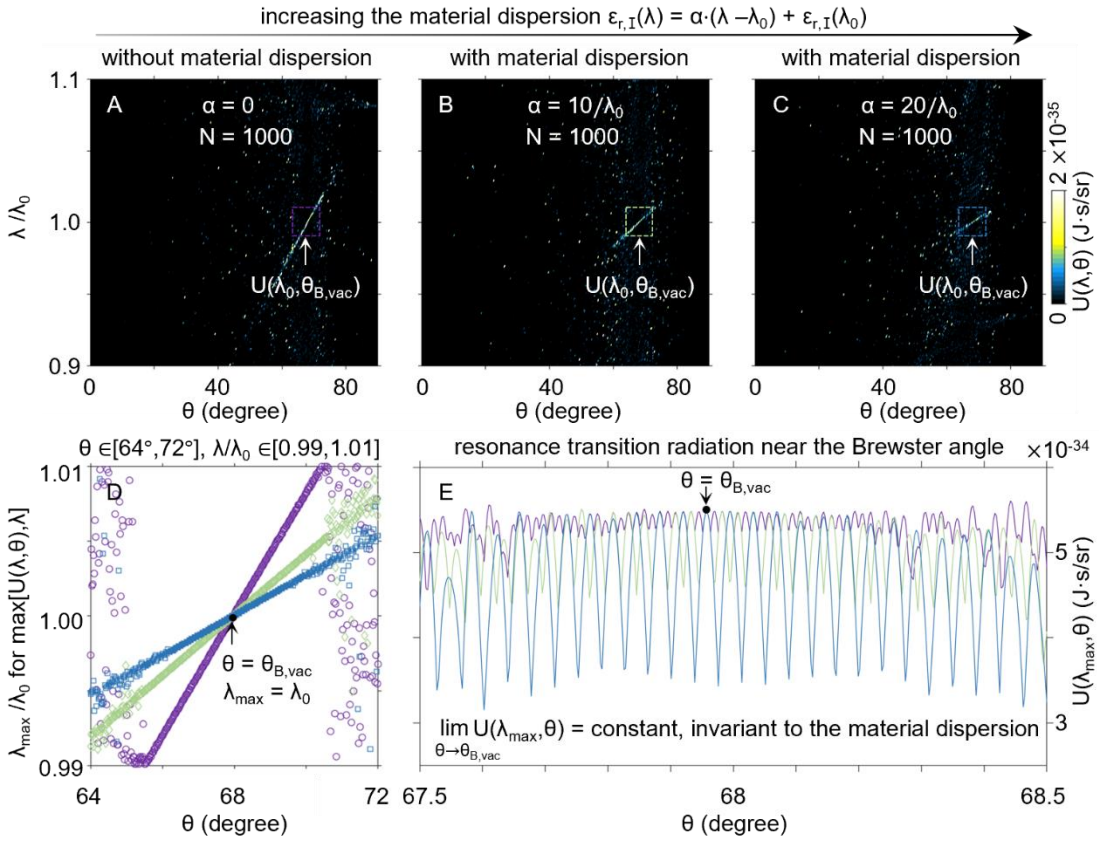

Fig. S8. Influence of the material dispersion on the resonance transition radiation via Brewster randomness. (*A*-*C*) Angular spectral energy density $U(\lambda, \theta)$ of free-electron forward radiation from layered aperiodic nanostructures with different material dispersion. For illustration, we set $\varepsilon_{\mathrm{r,I}}(\lambda) = \alpha(\lambda - \lambda_0) + \varepsilon_{\mathrm{r,I}}(\lambda_0)$, where α is a self-defined parameter to characterize the material dispersion and λ_0 is the predefined working wavelength in vacuum. For comparison, α is set to be 0 in (*A*), $10/\lambda_0$ in (*B*), and $20/\lambda_0$ in (*C*). The other setup is the same as that in Fig. 3*C* of the main text. (*D*) Dependence of $\lambda_{\max}$ on θ for various material dispersion, as extracted from (*A*-*C*), where $U(\lambda_{\max}, \theta) = \max[U(\lambda, \theta), \lambda]$. (*E*) Dependence of $U(\lambda_{\max}, \theta)$ on θ. There is always the emergence of a radiation peak at the special point of $(\theta_{\mathrm{B,vac}}, \lambda_0)$, with its intensity and directionality unaffected by the material dispersion.

S4.3 Influence of the material loss

In this subsection, we investigate the influence of material loss on the performance (e.g. the intensity and directionality) of resonance transition radiation via Brewster randomness at a predefined single wavelength

$\lambda = \lambda_0$ in Fig. S9*A*-*D*. On the one hand, we would like to highlight that there are many low-loss materials, whose loss tangent $\tan\delta = \mathrm{Im}(\varepsilon_{\mathrm{r,X}})/\mathrm{Re}(\varepsilon_{\mathrm{r,X}})$ can be down to 10^{-5} [10-13], namely $\tan\delta \leq 10^{-5}$. Under this scenario, the material loss has negligible influence of the performance of resonance transition radiation, even when the interface number N increases up to 10^4, as shown in Fig. S9 *A*, *B* and *D*. On the other hand, when the material loss is relatively large (e.g. $\tan\delta = 10^{-4}$ or 10^{-3} in Fig. S9 *A*, *C* and *D*), the material loss would have non-negligible influence on the performance of resonance transition radiation. To be specific, when the interface number N increases in Fig. S9*A*, the intensity of resonance transition radiation would first increase and later saturate. For example, when $\tan\delta = 10^{-3}$ in Fig. S9*C*, the intensity of resonance transition radiation would become relatively insensitive to the variation of N when $N \geq 200$. This is mainly because when N is large enough, only the resonance transition radiation created at a certain number of interfaces close to the forward vacuum region will make the dominant contribution to the whole radiation, while the resonance transition radiation created from the other interfaces far away from the forward vacuum region could almost dissipate due to the propagation loss of emitted light inside the lossy materials and thus would make negligible contribution to the whole radiation. We further show in Fig. S9*D* that the directionality of resonance transition radiation follows a similar tendency with the radiation intensity. That is, the angular width $\Delta\theta_{\mathrm{FWHM}}$ would first decreases and later almost stabilize as N increases in Fig. S9*D*.

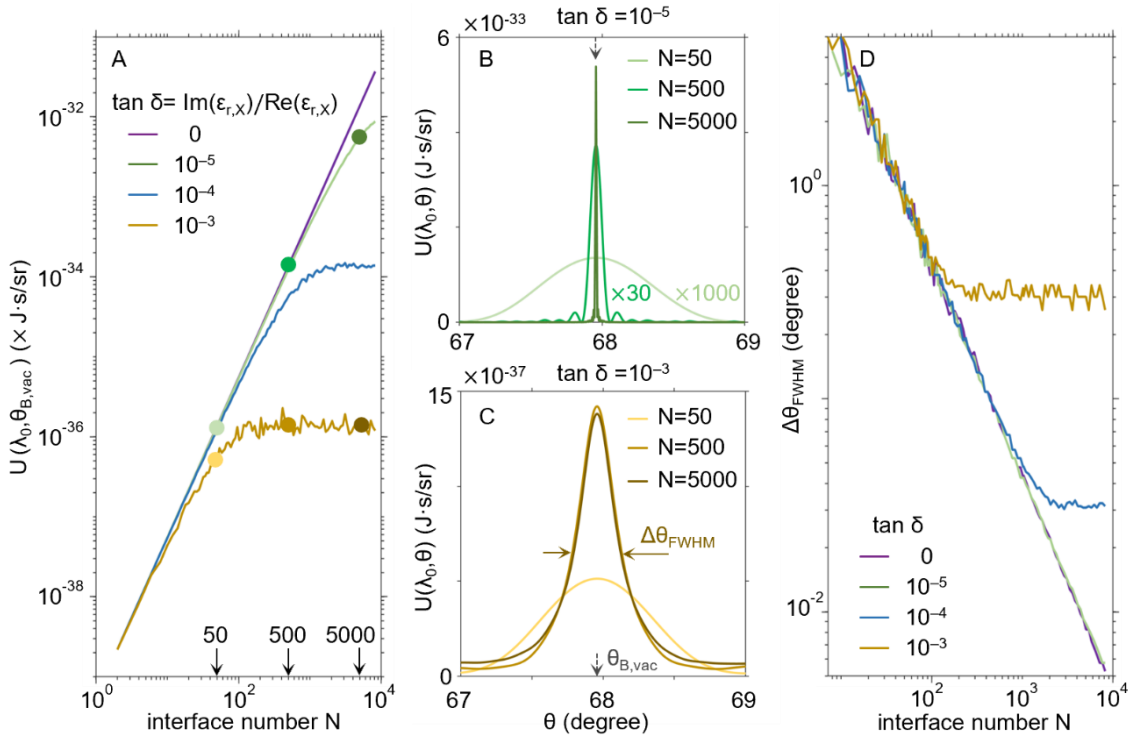

Fig. S9. Influence of the material loss on the resonance transition radiation via Brewster randomness. The

basic structural setup is the same as Fig. 3*C* in the main text. (*A*) Dependence of the angular spectral energy density $U(\lambda_0, \theta_{\mathrm{B,vac}})$ at the working wavelength $\lambda = \lambda_0$ and at the Brewster angle $\theta = \theta_{\mathrm{B,vac}}$ on the interface number N under different material losses, with the loss tangent $\tan\delta$ varying form 0, 10^{-5}, 10^{-4} to 10^{-3}. (*B* and *C*) Angular spectral energy density of $U(\lambda_0, \theta)$ at the working wavelength $\lambda = \lambda_0$ for various interface numbers, namely $N = 50$, 500 or 5000. For instance, we set $\tan\delta = 10^{-5}$ in (*B*) and $\tan\delta = 10^{-3}$ in (*C*). (*D*) Dependence of the angular width $\Delta\theta_{\mathrm{FWHM}}$ on the interface number N with various material losses.

S4.4 Influence of the interface number

In this subsection, we further investigate the influence of interface number on three types of radiation peaks in Fig. S10*A*-*E*. As background, the radiation peaks in the λ - θ parameter space are categorized into three types. First, the appearance of most radiation peaks is intrinsically random and sensitive to the variation of Brewster randomness. Second, when $\lambda \to \lambda_0$ and $\theta \to \theta_{\mathrm{B,vac}}$, the appearance of radiation peaks becomes relatively insensitive to the variation of Brewster randomness. Third, strictly speaking, only the radiation peak at the special point of $(\theta_{\mathrm{B,vac}}, \lambda_0)$ is invariant to the variations of Brewster randomness. As suggested, we further investigate the influence of interface number on these three types of radiation peaks in Fig. S10*A*-*E*. From Fig. S10 *D* and *E*, we safely argue that the appearance of both the second and third types of radiation peaks are relatively insensitive to the variation of the interface number. By contrast, as the interface number increases, there would be more first-type radiation peaks emerging in the λ - θ parameter space in Fig. S10*A*-*C*. Moreover, when the interface number is large enough in Fig. S10*C*, the first-type radiation peaks are inclined to show up near the Brewster angle.

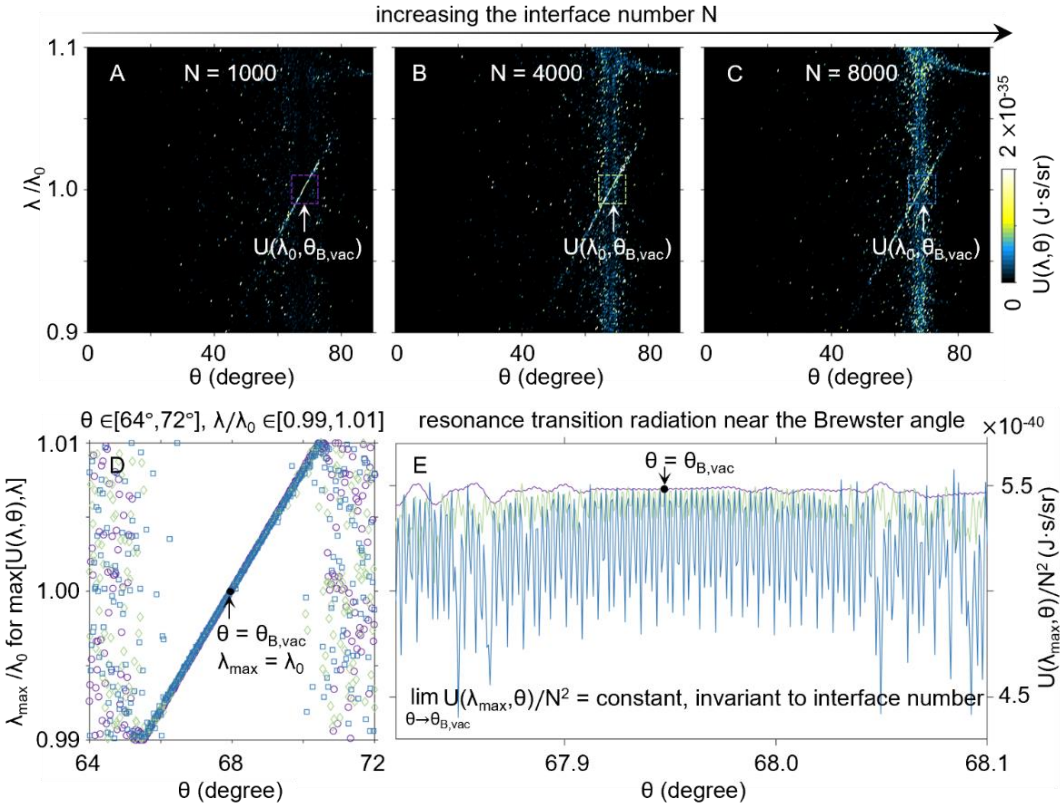

Fig. S10. Influence of the interface number N on the resonance transition radiation via Brewster randomness. The structural setup here is the same as Fig. 3*C* in the main text, except for N. Here $N = 1000$, 4000 and 8000 in (*A*)-(*C*) respectively. (*A*)-(*C*) Angular spectral energy density $U(\lambda, \theta)$ of free-electron forward radiation from layered aperiodic nanostructures via Brewster randomness in the λ - θ parameter space (*D*) Dependence of $\lambda_{\max}$ on θ for various interface numbers, as extracted from (*A*-*C*), where $U(\lambda_{\max}, \theta) = \max[U(\lambda, \theta), \lambda]$. (*E*) Dependence of the normalized radiation intensity $U(\lambda_{\max}, \theta)/N^2$ on θ. The value of $U(\lambda_0, \theta_{\mathrm{B,vac}})/N^2$ is a constant, which is invariant to the interface number.

S4.5 Photon yield of resonance transition radiation via Brewster randomness

In this subsection we derive the photon yield of resonance transition radiation via the Brewster randomness, namely the number of photons generated per unit length $\frac{\partial N_{\mathrm{photon}}}{\partial L}$. We show in Fig. S11 the total photon number generated per unit length per wavelength $\frac{\partial^2 N_{\mathrm{photon}}}{\partial L \partial \lambda}$ as a function of the wavelength λ within the regime of $\lambda/\lambda_0 \in [0.99,1.01]$. From Fig. S11, the value of $\frac{\partial^2 N_{\mathrm{photon}}}{\partial L \partial \lambda}$ from the resonance transition radiation via Brewster randomness is comparable to that from the conventional Cherenkov radiation inside dilute gases (e.g. those with a refractive index $n = 1.002$). By integrating $\frac{\partial^2 N_{\mathrm{photon}}}{\partial L \partial \lambda}$ within the wavelength regime of

$\lambda/\lambda_0 \in [0.99,1.01]$, we can obtain the photon yield, namely $\frac{\partial N_{\text{photon}}}{\partial L} = \int_{\lambda_0-\Delta\lambda}^{\lambda_0+\Delta\lambda} d\lambda \frac{\partial^2 N_{\text{photon}}}{\partial L \partial \lambda}$, where $\Delta\lambda/\lambda_0 = 0.01$. To be specific, the photon yield from the resonance transition radiation via Brewster randomness is 5.98 photons per meter, while the photon yield from the conventional Cherenkov radiation in the dilute gas is 7.33 photons per meter. On the other hand, we would like to highlight that while the potential inelastic electron scattering may occur during the interaction between swift electrons and the designed sample, one feasible route is to avoid the inelastic electron scattering is to drill a tiny hole with its center along the electron trajectory [14,15] in Fig. S12. Under this scenario, the evanescent wave carried by swift electrons can still well interact with the designed sample, while the swift electrons themselves will not directly interact with the sample and thus can safely penetrate through the sample.

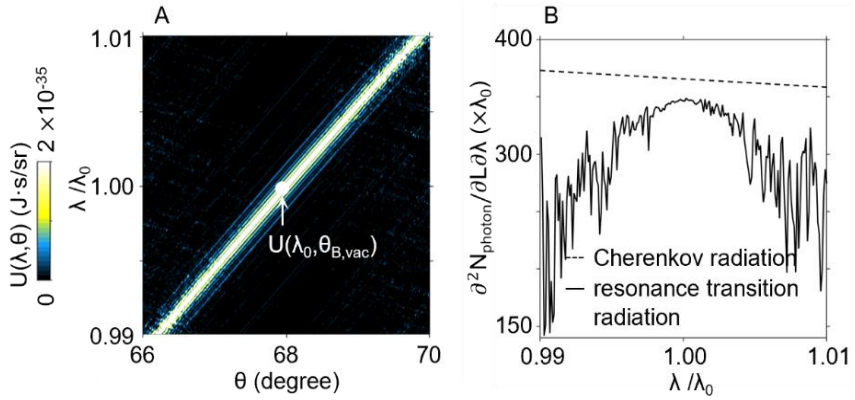

Fig. S11. Photon yield of resonance transition radiation via Brewster randomness. The structural setup is the same as that in Fig. 3*C* of the main text. (*A*) Angular spectral energy density $U(\lambda,\theta)$ of free-electron resonance transition radiation via Brewster randomness in the wavelength regime of $\lambda/\lambda_0 \in [0.99,1.01]$. (*B*) Total photon numbers per unit length per wavelength $\frac{\partial^2 N_{\text{photon}}}{\partial L \partial \lambda}$, where the photon number is calculated according to $N_{\text{photon}} = \int_{\lambda_0-\Delta\lambda}^{\lambda_0+\Delta\lambda} d\lambda \int_0^{\frac{\pi}{2}} d\theta\, U(\lambda,\theta)/(\hbar\lambda) \cdot (2\pi\sin\theta)$. Mathematically, we have $\frac{\partial^2 N_{\text{photon}}}{\partial L \partial \lambda} = \frac{\partial^2 N_{\text{photon}}}{\partial N_{\text{interface}} \partial \lambda} \cdot \frac{2}{\langle d_{\text{I}} \rangle + \langle d_{\text{II}} \rangle}$, where $\frac{\partial^2 N_{\text{photon}}}{\partial N_{\text{interface}} \partial \lambda}$ is the total photon number generated per interface per wavelength [2,16], $N_{\text{interface}}$ is the interface number, and $\langle d_{\text{X}} \rangle$ is the average thickness of the layer composed of dielectric X. Without loss of generality, here we set d_{X} to be the minimum Brewster thickness, namely $d_{\text{X}} \equiv d_{\text{B,X}}$ (see the definition of $d_{\text{B,X}}$ in equation (3) of the main text). For example, $d_{\text{B,I}} = 0.48\lambda_0$ and $d_{\text{B,II}} = 0.17\lambda_0$ are used in the calculation here. For comparison, the photon yield of conventional Cherenkov radiation from dilute gases with the refractive index of $n = 1.002$ [16] is also shown. By integrating

$\frac{\partial^2 N_{\text{photon}}}{\partial L \partial \lambda}$ within this wavelength regime of interest, we obtain the photon yield $\frac{\partial N_{\text{photon}}}{\partial L}$ from the resonance transition radiation via Brewster randomness is 5.98 photons per meter, while the photon yield from the conventional Cherenkov radiation in dilute gases is 7.33 photons per meter.

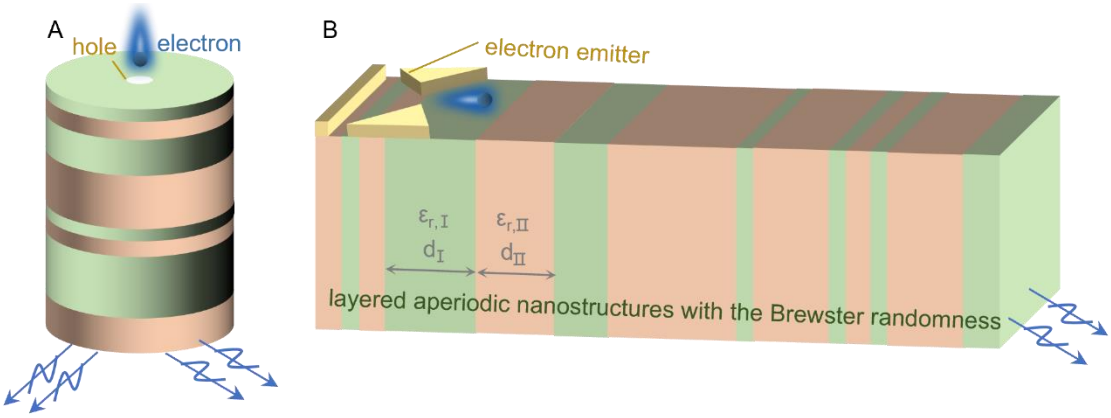

Fig. S12. Structural setup for possible experimental realization. For the safe penetration of electrons through the designed layered structure, a small hole can be drilled along the electron trajectory as shown in (*A*) [14,15]. For better integration, we may integrate the electron emitter directly on one side wall of the nanostructure in (*B*) so that the electrons can move with a very small vertical distance to the nanostructure [17]. For the scheme in (*B*), the emitted photons are collected in the lower side, which is highlighted by the blue arrows.

S4.6 Resonance transition radiation via Brewster randomness by using layered nanostructures composed of realistic materials

In this subsection, we show the resonance transition radiation via Brewster randomness in Fig. S13 by using a layered nanostructure composed of realistic materials [10-13], such as SiO_2 [10] with a relative permittivity $\varepsilon_{\text{r,SiO}_2}(\lambda_0) = 2.1$ and Cytop glass [13] with a relative permittivity $\varepsilon_{\text{r,Cytop}} = 1.8$, where the working wavelength is set to be $\lambda_0 = 500$ nm. In addition, in order to consider the potential influence of material loss, the loss tangent of both low-loss materials is set to be $\tan\delta = 10^{-5}$.

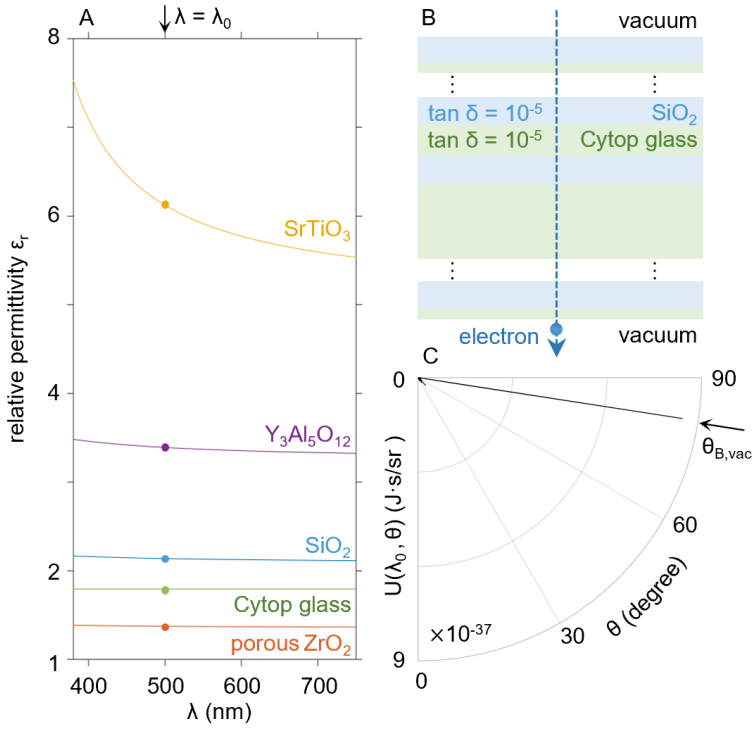

Fig. S13. Resonance transition radiation via Brewster randomness from a layered nanostructure composed of realistic materials. (*A*) Dependence of the relative permittivity of $\varepsilon_{\mathrm{r}}(\lambda)$ on the wavelength for some realistic materials [10-13]. As denoted by the solid circles in (*A*), $\varepsilon_{\mathrm{r,SrTiO_3}}(\lambda_0) = 6.1$, $\varepsilon_{\mathrm{r,Y_3Al_5O_{12}}}(\lambda_0) = 3.4$, $\varepsilon_{\mathrm{r,SiO_2}}(\lambda_0) = 2.1$, $\varepsilon_{\mathrm{r,Cytop}} = 1.8$, and $\varepsilon_{\mathrm{r,ZrO_2}}(\lambda_0) = 1.4$ at the working wavelength $\lambda_0 = 500$ nm. These materials have very low loss, whose loss tangent are generally down to 10^{-5} in the visible spectrum, namely $\tan\delta = \mathrm{Im}(\varepsilon_{\mathrm{r,X}})/\mathrm{Re}(\varepsilon_{\mathrm{r,X}}) \leq 10^{-5}$. (*B*) Structural schematic of resonance transition radiation from layered nanostructures. For illustration, SiO_2 [10] and Cytop glass [13] are chosen to construct the layered nanostructure. In addition, we artificially set the loss tangent to be 10^{-5} in the calculation. The other setup is the same as that in Fig. 3*C* in the main text. (*C*) Angular spectral energy density of free-electron forward radiation at the working wavelength $\lambda = \lambda_0$. From (*C*), there is a strong and sharp radiation peak at the Brewster angle $\theta = \theta_{\mathrm{B,vac}}$.

Reference:

1. V. L. Ginzburg, I. M. Frank, Radiation of a uniformly moving electron due to its transition from one medium into another. *Journal of Physics (USSR)* **9**, 353-362 (1945).
2. V. L. Ginzburg, *Transition radiation and transition scattering* (A. Hilger, 1990).
3. Z. Gong, *et al.*, Interfacial Cherenkov radiation from ultralow-energy electrons. *Proceedings of the National Academy of Sciences of the USA* **120**, e2306601120 (2023).
4. X. Lin, *et al.*, Controlling Cherenkov angles with resonance transition radiation. *Nat. Phys.* **14**, 816-821 (2018).
5. R. Chen, *et al.*, Free-electron Brewster-transition radiation. *Sci. Adv.* **9**, eadh8098 (2023).
6. J. Chen, *et al.*, Low-velocity-favored transition radiation. *Phys. Rev. Lett.* **131**, 113002 (2023).

7. K. Kim, *et al.*, Massively parallel ultrafast random bit generation with a chip-scale laser. *Science* **371**, 948-952 (2021).
8. J. E. Sipe, P. Sheng, B. S. White, M. H. Cohen, Brewster anomalies: a polarization-induced delocalization effect. *Phys. Rev. Lett.* **60**, 108 (1988).
9. A. A. Asatryan, *et al.*, Suppression of Anderson localization in disordered metamaterials. *Phys. Rev. Lett.* **99**, 193902 (2007).
10. E. D. Palik, *Handbook of optical constants of solids* (Academic press, 1998).
11. A. Pirvaram, N. Talebzadeh, M. Rostami, S. N. Leung, P. G. O'Brien, Evaluation of a ZrO2/ZrO2-aerogel one-dimensional photonic crystal as an optical filter for thermophotovoltaic applications. *Thermal Science and Engineering Progress* **25**, 100968 (2021).
12. J. Hrabovský, M. Kučera, L. Paloušová, L. Bi, M. Veis, Optical characterization of Y3Al5O12 and Lu3Al5O12 single crystals. *Opt. Mater. Express* **11**, 1218-1223 (2021).
13. K. Leosson, B. Agnarsson, Integrated biophotonics with CYTOP. *Micromachines* **3**, 114-125 (2012).
14. G. Adamo, *et al.*, Light well: A tunable free-electron light source on a chip. *Phys. Rev. Lett.* **103**, 113901 (2009).
15. Z. Dang, *et al.*, Chiral Smith-Purcell Radiation Light Source. *Adv. Opt. Mater.* **11**, 2300274 (2023).
16. J. A. Kong, *Electromagnetic wave theory* (EMW Publishing, 2008).
17. F. Liu, *et al.*, Integrated Cherenkov radiation emitter eliminating the electron velocity threshold. *Nat. Photonics* **11**, 289-292 (2017).